2017-01-01

Molecular Dynamics Studies Of Crystal Growth Phenomena In CDTE Based Heterostructures

Rodolfo Aguirre II
University of Texas at El Paso, raguirre4@miners.utep.edu

MOLECULAR DYNAMICS STUDIES OF CRYSTAL GROWTH PHENOMENA IN CDTE BASED HETEROSTRUCTURES

RODOLFO AGUIRRE II

Doctoral Program in Electrical and Computer Engineering

APPROVED:

David Zubia, Ph.D., Chair

Xiaowang Zhou, Ph.D., Co-Chair

John McClure, Ph.D.

Stella Quinones, Ph.D

Charles Ambler, Ph.D.
Dean of the Graduate School

Dedication

To my Dad, Mom, Brother, Sisters and Myself …

MOLECULAR DYNAMICS STUDY OF POLY AND MONOCRYSTALLINE CDS/CDTE JUNCTIONS AND CU DOPED ZNTE BACK CONTACTS FOR SOLAR CELL APPLICATIONS

by

RODOLFO AGUIRRE II, BSEE, MSEE

DISSERTATION

Presented to the Faculty of the Graduate School of

The University of Texas at El Paso

in Partial Fulfillment

of the Requirements

for the Degree of

Doctor of Philosophy

Department of Electrical and Computer Engineering

THE UNIVERSITY OF TEXAS AT EL PASO

May 2017

Acknowledgements

I would like to acknowledge my family, friends and mentors who supported me through the completion of the doctoral degree. Specifically, I would like to thank Dr. David Zubia for all his guidance, knowledge and encouragement. Also, special thanks to Dr. Xiaowang Zhou and Dr. Jose Chavez for teaching me the computational tools required for the completion of my work. Also, I would like to thank my colleagues Sergio Almeida, Aldo Vidana, Arka Talukdar, Jose Valdez, Karla Tarango and Mariana Martinez for sharing all their knowledge and experiences with me. Additionally, I would like to thank my Mom and Dad for providing me a place to live during my studies, my brother Brandon for giving me advice, my sister Zoe for providing me affection and love, and my sister Maria for inspiring me. I would like to thank UTEP for making high education available to families with low income. I would like to thank the Solar Economy IGERT fellowship program for funding me through my doctoral studies, as well as XEROX scholarship, Robert Amezcua scholarship, UTEP's travel funds and the Dean of the College of Engineering for providing me with funding for my final semester as a Ph. D. candidate. Finally, I would like to acknowledge XSEDE computational resources for awarding allocations for solar cell research and also thanks to Nito Gumataotao for helping me answering question regarding parallel computing and general linux system commands.

Abstract

Cadmium telluride (CdTe) is a material used to make solar cells because it absorbs the sunlight very efficiently and converts it into electricity. However, CdTe modules suffer from degradation of 1% over a period of 1 year. Improvements on the efficiency and stability can be achieved by designing better materials at the atomic scale. Experimental techniques to study materials at the atomic scale, such as Atomic Probe Tomography (APT) and Transmission Electron Microscope (TEM) are expensive and time consuming. On the other hand, Molecular Dynamics (MD) offers an inexpensive and fast computer simulation technique to study the growth evolution of materials with atomic scale resolution. In combination with advance characterization software, MD simulations provide atomistic visualization, defect analysis, structure maps, 3-D atomistic view, and composition profiles. MD simulations help to design better quality materials by predicting material behavior at the atomic scale.

In this work, a new MD method to study several phenomena such as polycrystalline growth of CdTe-based materials, interdiffusion of atoms at interfaces, and deposition of a copper doped ZnTe back contact is established. Results are compared with experimental data found in the literature and experiments performed and shown to be in remarkably good agreement.

Table of Contents

List of Tables

List of Figures

Chapter 1: Introduction

Sunlight has by far the highest theoretical potential of the earth's renewable energy sources and its energy is 10,000 times greater than the world's energy consumption estimated by 2050 [1]. Therefore, it is important to optimize solar cell technologies and exploit its usage. Photovoltaic cells are devices made out of layers of different materials that convert the sunlight directly into electricity. For example, CdTe is a material used for the fabrication of thin film photovoltaics due to its ideal optoelectronic properties and low manufacturing cost. Much improvement in the efficiency of CdTe-based solar cells was achieved from 1990 to 2010 resulting in record efficiencies up to 20%. However, theoretical research work shows that there is still a 10% room for improvement. More recently, enhancements on material quality at the atomic scale have increased the solar cell efficiency up to 22.1% [2] and have confirmed new pathways to increase CdTe solar cell efficiency to theoretical values. Most of these developments have been focused on the study of CdTe at the atomic scale.

Chapter 2: Technical Background

2.1 Overview

CdTe solar cells convert light into energy very efficiently [3] and have the lowest manufacturing cost among all solar cell technologies [4]. However, the solar cell efficiency is ~7% below its theoretical maximum [5] mainly due to problems in the material. Changes in material composition due to dopant concentration, defects and interdiffusion between the layers causes the formation of compensating extrinsic or intrinsic donor-type defects in the CdTe, thus decreasing hole concentration [6] [7]. Low p-CdTe hole concentration (10^{14} – 10^{15} cm^{-3}) results in lower junction band bending and difficulty in making an ohmic contact. This contributes to a lower open circuit voltage and therefore lower efficiency [7]. There has been significant effort to increase hole concentration in CdTe (10^{16}-10^{17} cm^{-3}) by adding different dopants such as Cu [6], As [8], P [9], and Cl [10], however little attention has been put on the structural mechanisms for doping CdTe. For example, little is known about how dopants diffuse through the lattice grain boundaries and other defects. It is believed that when doping CdTe, dopant atoms substitute Cd atoms and also form interstitial sites [11]. It is also believed that for silicon, dopant atoms segregate to non-coherent high angle grain boundaries more than they do to coherent low angle grain boundaries [12]; however there has not been a thorough study and understanding of how dopants are incorporated into the CdTe matrix. Moreover, the study of the growth mechanisms for polycrystalline CdTe has received much attention lately because of the use of polycrystalline CdTe material for the construction of high efficiency solar cells [13].

2.2 Survey of CdTe material

Cadmium telluride (CdTe) is a semiconductor compound mainly used for photovoltaics and sensors. CdTe belongs to the group II (Cd) and group VI (Te) from the periodic table, therefore sometimes it is referred to as a II-VI semiconductor. In comparison to silicon, CdTe has a lower manufacturing cost [4]. However, tellurium is a relatively scarce element [14], therefore ways to recycle Te from the CdTe modules have been investigated [15]. CdTe is either joined with cadmium sulfide (CdS) to form a solar cell or alloyed with mercury (Hg) or zinc (Zn) to build x-ray and gamma ray detectors [16], respectively. CdTe can be stable either in the zincblende or the wurtzite phases, which means it can have either a cubic or a hexagonal crystal structure depending on the strain applied and other thermodynamic forces present during crystal growth [17]. It has a lattice parameter of 6.48 Å [18] in the zincblende structure. The lattice parameter in the wurtzite structure is still debatable but theoretical calculations have obtained c = 7.451 Å and a = 4.55 Å [17]. The CdTe zincblende structure consist of Cd atoms occupying the sites as if it was an fcc structure and the Te atoms then are interpenetrated inside the Cd fcc structure. CdTe has 4 first-nearest neighbors and 12 second-nearest neighbors. CdTe is a direct bandgap semiconductor which yields a high absorption coefficient ($>10^4$ cm^{-1}) [19] which makes it suitable for photoelectronic applications. It has an energy bandgap of 1.5 electron volts (eV) [20] which is close to optimum for photovoltaic conversion of the solar electromagnetic spectrum.

2.3 Doping of CdTe for solar cell applications

Doping the CdTe with acceptor impurities is difficult due to self-compensation. Compensation is the ability for the material to reverse the process of doping by creating defects. CdTe self-compensation occurs mainly via Cd interstitials (Cd_i), Te vacancies (V_{Te}) and Te-Cd antisites (Te_{Cd}) [21]. If an extrinsic dopant is introduced, other states are then created that compensate the dopant type. For example, P is known to introduce acceptor impurities by

substituting Te (P_{Te}) but at the same time introducing P interstitials (P_i) which are donor impurities [22]. First principles studies indicate that Cu replaces Cd atoms in CdTe by forming Cu_xTe molecules which are acceptor dopants [23, 24]. However, recent studies show that Cu atoms segregate forming clusters either at the CdTe bulk or at the grain boundaries even at low concentration of Cu [25, 26].

Although copper has been used to dope champion polycrystalline CdTe solar cells with the highest record efficiencies, it is not the definitive dopant due to it producing hole concentrations only up to 10^{15} cm^{-3} [22] and its fast diffusion which cause instability issues. Cu is a highly mobile particle in CdTe and it deteriorates the electronic properties of the overall solar cell over time by diffusing to the junction between CdS and CdTe and causing a short circuit [27, 28]. Diffusion to the junction is higher in polycrystalline solar cells compared to single crystal material. Cu atoms are suspected to travel faster across defects such as dislocations and grain boundaries in comparison to the diffusion through the bulk. It is still unclear in which types of grain boundaries or dislocations, Cu has a higher or a lower diffusion.

In addition to diffusion, Cu is known to alter the structure of crystal matrices including grain boundaries and dislocation distribution. A change in structure means a change of the electronic properties and, therefore, a change in the efficiency of the solar cell. One example is Cu clustering. However information about how these clusters form or their size after deposition is lacking.

Due to these issues, phosphorous has been recently used as to replace Cu. However, Cu exists naturally in the production of CdTe since pure Cd and Te are byproducts of copper refining [29]; therefore it is difficult to completely remove Cu from CdTe. In conclusion, it is important to study the structural characteristics of Cu incorporation into the CdTe via bulk and defects to determine which pathways to take in the development of new generation solar cells with optimum morphology.

2.4 Monocrystalline vs Polycrystalline CdTe

Growth of Polycrystalline CdTe is affordable and easily achieved using closed space sublimation (CSS) [30], electron beam deposition [31], and thermal evaporation [32]. On the other hand, the growth of monocrystalline CdTe requires complex techniques such as vertical the Bridgman method [9] or Traveller heating method [33]. It has been demonstrated that high-efficiency CdTe solar cells can be obtained by using polycrystalline CdTe [34]. However, open circuit voltage above 1 volt needs to be achieved in order to get the full potential of polycrystalline cells. On the other hand, monocrystalline solar cells have shown open-circuit voltage higher than 1 volt while obtaining low efficiencies [9]. Many arguments have been made to justify the use of single crystal CdTe over polycrystalline such as the difficulty to dope polycrystalline CdTe and material quality limitations [13]. Given that polycrystalline CdTe solar cells are difficult to dope and have poor material quality, it is then not clear how high-efficiencies and very promising open-circuit voltages are obtained from these [5]. Defects in polycrystalline CdTe such as grain boundaries and dislocations have a major impact in the electronic properties of the overall solar cell.

Grain boundaries have been demonstrated to act as fast diffusivity paths for dopants [35]. Also, some grain boundaries could be electrically more active than other or not active at all [36]. Moreover, it has also been noticed that some grain boundaries are negatively charged by dopants and, therefore, they form localized p-n or p-n-p junctions with grain interiors. For example, Li *et. al.* found that CdTe grain boundaries with sufficient Cl segregation after the $CdCl_2$ treatment will negatively charge the boundary leading it to behave as an n-type region [37, 38]. Space charge built in these regions will help the separation of photo-generated carriers, thus reducing recombination.

Dislocations also facilitate the diffusion of dopants via pipe diffusion [39]. Dislocations found in polycrystalline CdTe have been identified but not limited to Lomer dislocations [40] and Shockley partial dislocations [38]. Stacking faults have been found to be bounded by grain boundaries [41], suggesting the presence of dislocations at the grain boundaries. Moreover,

threading dislocations (dislocations normal to the surface plane) have been found to connect the bulk to the interface [42].

In addition to dopant diffusion, it is important to study the growth, formation and motion mechanisms of dislocations and grain boundaries through the film. Moreover, dopant activation and post-treatments recrystallize and increase CdTe grain size [43] suggesting the motion of dislocations and grain boundaries.

2.5 Methods to study CdTe at the atomic scale

Transmission electron microscope (TEM) and atomic probe tomography (APT) are two commonly used methods to study CdTe at the atomic scale. For example, Yan *et. al.* identified that CdTe contained lamellar twin boundaries and double-positioning twin boundaries using TEM micrographs [44] as shown in Figure 1. The TEM images were analyzed and converted to simulated structures for use in first-principles density-functional total energy calculations. The study concluded that double-positioning twin boundaries contain dangling bonds and as a result create defect states within the bandgap that can trap both electrons and holes.

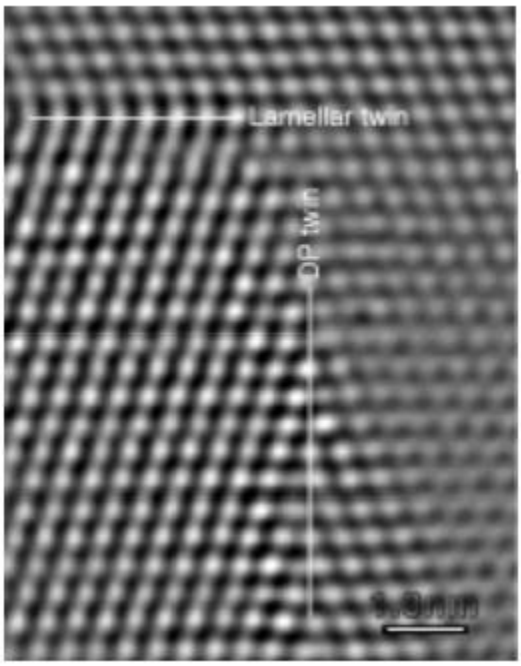

Figure 1: HRTEM image showing a lamellar twin boundary and a double-positioning twin boundary [44].

Similarly, APT studies by Wolden, *et. al.,* identified the atomic incorporation and growth of Cu in the CdTe [25]. The study shows copper clusters and suggests that the clusters promote the diffusion of other atoms such as Zn and Cd. Also, the study suggests that sequestration of Cu atoms by the clusters limits the amount of free Cu available to dope CdTe. APT image and composition profiles from this study are shown in Figure 2.

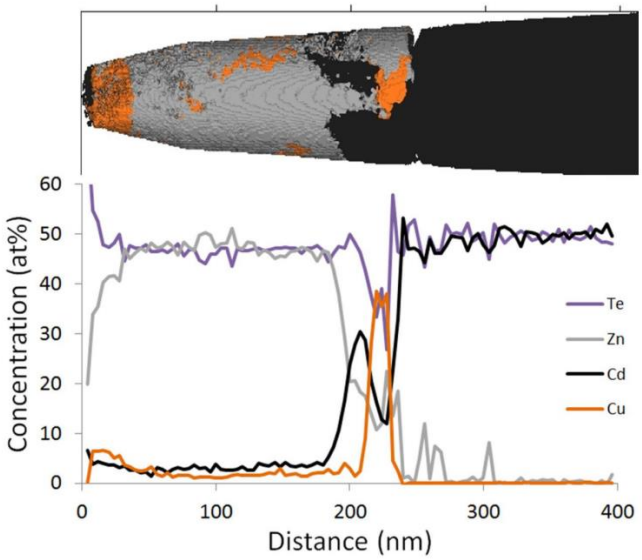

Figure 2: APT reconstruction through the as-deposited Cu-doped ZnTe/CdTe interface (top). 1D concentration profile of the elements (bottom) [25].

Another extremely useful technique to study the CdTe at the mesoscale is the time-of-flight (TOF) secondary-ion mass spectroscopy (SIMS) technique. The TOF SIMS technique gives a 3D composition representation of the sample and is an enhancement over the 1D SIMS technique. This technique is very suitable for the study of atomic composition and diffusion through polycrystalline and monocrystalline heterostructures. For example, Colegrove *et. al.* studied the diffusion of phosphorous in polycrystalline and monocrystalline CdTe [22]. Figure 3 (a) and (b) show the 2D lateral P-intensity map and 3D TOF-SIMS P-intensity tomography rendering of a monocrystalline sample. Similarly, Figure 3 (c) and (d) show the 2D lateral P-intensity map and 3D TOF-SIMS P-intensity tomography rendering of a polycrystalline sample. Together with theoretical calculations, these studies reveal two bulk-diffusion mechanisms controlling P dopant incorporation in CdTe. The first mechanism is substitutional diffusion by the P atoms replacing Te sites. The second mechanism is P atoms diffusing interstitially. Also, the P diffusion through the grain boundaries was found to be about 5 orders of magnitude greater than the bulk diffusion. This is confirmed by looking at the accentuated lines of Figure 3 (c) and

(d) indicated by the black circles. In comparison, the single crystal in Figure 3 (a) and (b) show shallower diffusion of P atoms.

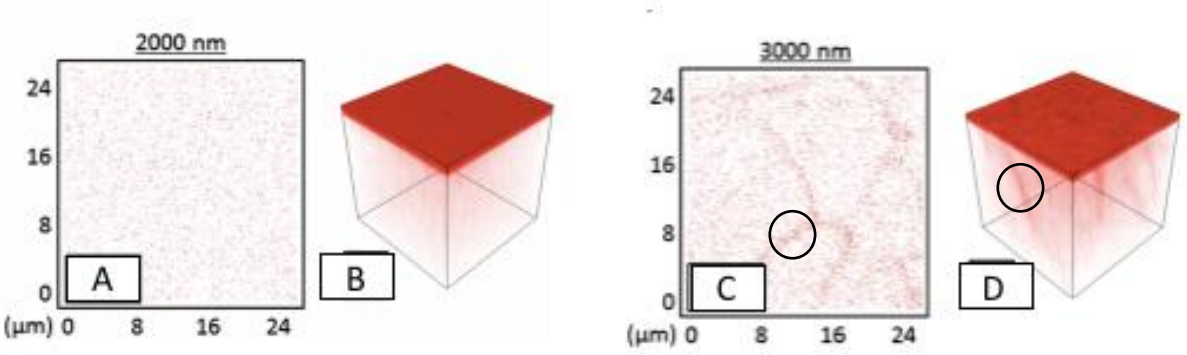

Figure 3: Time of flight SIMS reconstruction of P dopant in monocrystalline CdTe rendered in a) lateral 2D and b) 3D. Time of flight SIMS reconstruction of P dopant in polycrystalline CdTe rendered in c) lateral 2D and d) 3D [22].

Interestingly, diffusion through defects such as grain boundaries had not been studied in such detail before. TEM, APT and TOF SIMS capabilities are extremely useful and provide information that no other experimental characterization tool can provide. However, these techniques are complex and time consuming. Alternatively, molecular dynamics (MD) simulations, in conjunction with visualization techniques, offer 3D structural visualization and time evolution of the diffusion and growth of heterostructures at the atomic scale. In addition, MD simulations are practical and less expensive.

2.6 Molecular dynamics

Molecular dynamics is a simulation technique for studying the interactions of atoms in a system. Potential energy of the system is calculated using mathematical functions called interatomic potentials. Interatomic potentials are usually written as the series expansion of functional terms that depend on the position of one, two, three, or N atoms at a time. There are different types of interatomic potentials such as the Bond Order potential [45], Lennard-Jones potential [46], Stillinger-Weber (SW) potential [47], and others. In this work, the SW potential is

used for all simulations. The SW potential was developed by Frank H. Stillinger and Thomas A. Weber in 1985. Since then, it was widely used for the simulation of silicon and other elements. Recently, the SW potential has been used extensively in II-VI compounds because it ensures that the lowest energy structures are diamond-cubic, zinc-blende, or wurtzite [48]. The SW potential is based on two terms that represent the interaction between two particles and three particles respectively [49] as shown in the Equation 1, where θ_{jik} is the angle formed by the ij bond and the ik bond, and $g(r)$ is the decaying function with a cutoff between the first and the second neighbor shell.

$$V = \frac{1}{2}\sum_{ij} \phi(r_{ij}) + \sum_{ijk} g(r_{ij})g(r_{ik})(\cos\theta_{jik} + \frac{1}{3})^2$$

Equation 1: two-body term and three-body term of the Stillinger-Weber potential.

In a system of atoms, this interatomic potential is used in order to update the energy of every atom. Then, the forces acting upon each individual atom are derived from these energies. Similarly, their acceleration is determined by the net interatomic force divided by the atom's mass. The velocities can also be calculated by multiplying acceleration and time. Once the forces acting on the atoms are known, the positions of the atoms can be updated. Finally, the calculations are performed again for the new positions [50].

2.7 Other simulation techniques

Other simulation techniques include density functional theory (DFT) [51] which is a computational quantum mechanical modelling method used to investigate the electronic structure of materials. Generally, the DFT algorithm allows you to derive electronic information of defects including their formation energy and transition energy. The formation energy provides the

energy required for a specific defect to form and the transition energy represents the energy necessary for that specific defect to transition into another defect. Recent studies have used DFT to calculate these energies for different extrinsic and intrinsic defects formed when Cu and/or Cl are introduced in the CdTe [52]. For example, defects such as antisites (Cl_{Te} and Cu_{Cd}), vacancies (V_{Cd} and V_{Te}), and interstitials (Cl_i and Cu_i) were created artificially. Once the defects are created, DFT calculations are performed to calculate the energies. The resulting energies calculated are shown in Figure 4 (a). These studies can also be applied to grain boundaries. Applying DFT to grain boundaries give us information about which types of grain boundaries are electrically active. Knowing this, we can then evaluate which grain boundaries are beneficial for the overall solar cell. Also, we could apply different types of atoms to the grain boundaries in order to simulate segregation or clustering and do the same energy calculations. For example, in the same work by Yang, *et. al.*, different types of grain boundaries were artificially created. Cu and Cl atoms were added at different distances from the grain boundaries. Then, the energy was calculated as shown in Figure 4 (b).

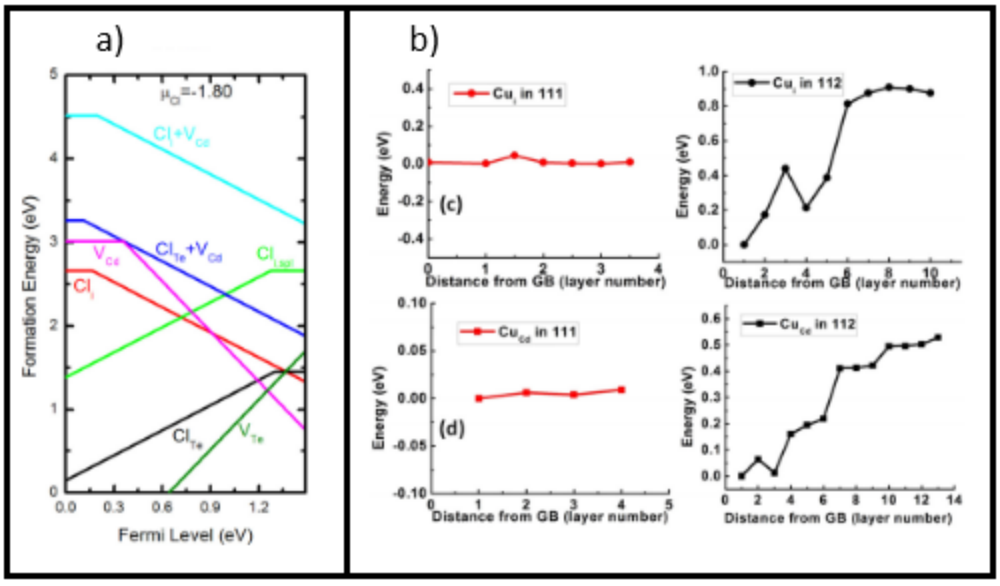

Figure 4: First principles calculations of a) Cl defect formation and b) Cu energy vs distance from grain boundary [52].

Chapter 3: Methodologies

3.1 Computational resources

The Large-scale Atomic/Molecular Massively Parallel Simulator (LAMMPS) [53] is a package developed and distributed by Sandia National Laboratories which runs Molecular Dynamics (MD) code. MD simulations used in this work were performed using LAMMPS. The code was installed at different computer clusters including Virgo high performance computer (HPC) which runs on a Beowulf Cluster with 160 cores, 2.65 GHz speed and 139 Peak GFLOP/s. Virgo cluster is situated at the Department of Electrical Engineering at the University of Texas at El Paso. Two other HPC servers were used for the simulations. First, the Gordon HPC with 16,384 cores, 2.6 GHz Speed and 341 Tflop/s. Second, the Stampede HPC with 522,080 cores, 2.4 GHz Speed and 2,200 Tflop/s. These two servers were awarded as part of the Nanomil's team startup package provided by the Extreme Science and Engineering Discovery Environment resources. Other resources previously used that also had an impact on this work include Red Sky with 22,768 cores, 293 GHz Speed and 264 Tflop/s. Chama with 19,712 cores, 2.6 GHz Speed amd 392 Tflop/s and Sky Bridge with 29,568 cores, 2.6 GHz speed, and 600 Tflop/s.

3.1 MD simulations conditions

Single crystal simulations were carried out by using an initial zinc blende CdTe substrate containing six monolayers in the [111] growth direction (Y axis). The substrate was created with a lattice constant of a = 6.478 A. Periodic boundary conditions were used in the in-plane directions (X and Z axes). Deposition temperature was mainly 1200 K with a few exceptions where temperature used was 1400 K for comparison. Total deposition time was mainly 42.4 ns with a few cases where more or less deposition time was used for comparison. Deposition rate is ~0.002 A/ps for all simulations.

3.1 Data visualization and post-processing

Three dimensional time evolved visualization of simulated data including atomic species maps, structure maps, and dislocations maps were generated using the Open Visualization Tool (Ovito) [54]. Ovito is a scientific visualization and analysis software for atomistic simulation data developed by Alexander Stukowski at Darmstadt University of Technology, Germany. The program is open-source and freely available for all major platforms. Post analysis of simulated data includes the generation of composition profiles, calculation of surface roughness, production of structural composition profiles, and calculation of number of wrong bonds. Post analysis was performed using Matlab software. Matlab is a numerical computing environment and programming language. Additional analysis and reports were done using Microsoft Office.

3.2 Diffusion Analysis

In order to analyze the diffusion between the structures, it was necessary to construct elemental profiles that show the distribution of specific atoms throughout the films. For this, an algorithm was created to count the number of atoms in the Y direction from the LAMMPS exported simulation generated file to MATLAB. The algorithm creates a 3D step box with fixed length and width as represented in the red box of Figure 5 (a). Then, the algorithm counts the number of atoms inside the step box and divides them by the volume of the step box. Blue filled circles in Figure 5 represent the atoms counted by the step box while white filled circles represent the atoms that are located outside the box, and therefore, are not counted by the step box. Partially filled circles represent atoms right at the edge of the step box. The algorithm stores the volumetric concentration of the step box in the initial position and then the step box moves to the next position as seen in Figure 5 (b). In this next position, the algorithm performs the same calculation and moves to the following position. Eventually, the step box moves across the sample, stores each volumetric concentration and constructs a plot of the volumetric concentration versus position.

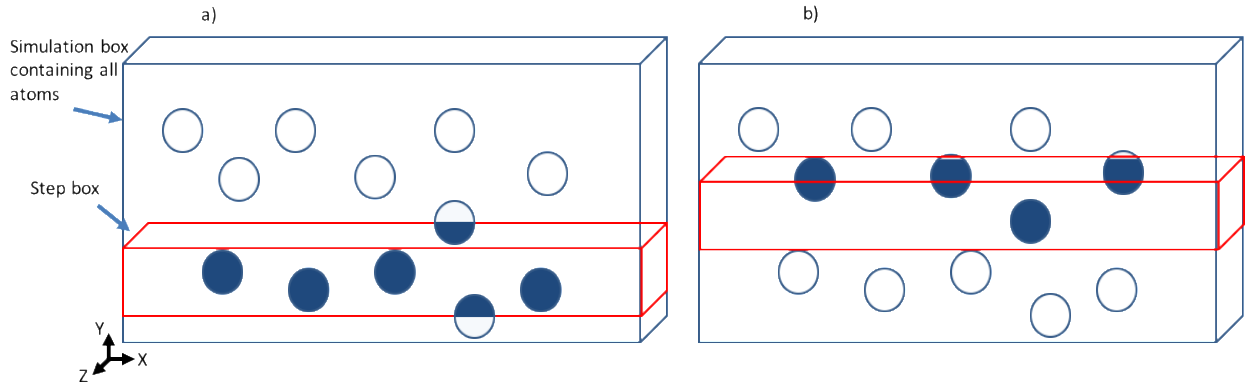

Figure 5: Visual representation of the compositional profile algorithm.

First trials of the algorithm showed composition profiles to have very few data points. This was mainly due to the step box being too big. By setting the step size close to the interplanar distance, smoother graphs were obtained. However, there was still some variation in the compositional profiles, specifically on the samples with more atomistic disorder. This was mainly due to the uneven distribution of atoms within the box. To solve this, an algorithm was implemented to randomly displace the atom positions within the step size. The compositional profile was improved even further with this implementation. However, the randomization of atom positions varied from run to run. In consequence, the composition profile had a slight change from run to run. To overcome this situation, randomization of the original data was performed for over 500 times. The final composition profile was the highly converged average representation of all the randomizations.

The diffusion between the layers can then be quantified by obtaining diffusion coefficients. The diffusion coefficients of Cd, Zn, and Cu were determined by fitting a complementary error function to the data outside the regions of interfacial roughness. To obtain an estimate of both activation energy Q (eV) and pre-exponential factors, D_0 (A^2/ps), independent diffusion simulations were performed at Sandia National Labs by Dr. Xiaowang Zhou using an establish approach reported in Ref [55]. In these simulations, simulated annealing is performed at different temperatures for samples with different vacancy concentrations. The

mean square displacement of diffusion species is used to calculate diffusivities, and the diffusivities at different temperatures are fitted to Arrhenius equation to obtain activation energy and pre-exponential factor. Highly converged Arrhenius fits were achieved at the extremely long simulation time of 1000 ns. One useful result that can be applied here is that the activation energy is independent of the vacancy concentration whereas the pre-exponential factor is proportional to the vacancy concentration. Using a $Cu_{0.1}Zn_{0.9}Te$ sample, we found that the activation energies for Cu, Zn, and Te diffusion are respectively 2.8, 1.9, and 1.9 eV. Given the diffusivities fitted from the simulations and the activation energies determined, the pre-exponential coefficients were also determined.

Finally, the root mean squared (RMS) roughness was calculated by finding the maximum atom in the Y position within a region defined by dy and dz. A three-dimensional representation of the roughness was produced by creating a grid using the data of the maximum positions of the atoms.

Chapter 4: Results

4.1 Growth of layered ZnTe/Cu/CdTe

The growth of layered ZnTe/Cu/CdTe is motivated by experiments found in the literature [27]. These experiments investigated the change in electrical characteristics of the CdTe solar cell using different Cu loadings. This section will show the growth of the ZnTe/Cu/CdTe heterostructure at Cu loadings of 0.0 ML, 0.3 ML and 8.0 ML which are close to experimental loadings. First, the growth of a monocrystalline CdTe substrate used for the depositions of Cu and ZnTe is described. Then, the subsequent Cu and ZnTe growths will be described.

4.1.1 Single Crystal (SX) CdTe growth

The CdTe substrate consisted of a single crystal CdTe film grown to a thickness of 150 Å on a thin (~6 monolayers) perfect [111] single crystal CdTe. The grown layer is shown in Figure 6 (a) and its structure identification along with dislocation types is shown in Figure 6 (b). The grown film shows a very well defined single crystal layer with the exception of horizontally oriented stacking faults and 1/6<112> Shockley partial dislocations bounding the stacking faults. Quantitatively, the grown film grew predominantly in the wurtzite (WZ) phase (52.4 at. %) following by the zincblende (ZB) (34.7 at. %) phase. The remaining 12.9% are "undetermined" atoms which mostly resides at defects and surfaces. This can be confirmed by observing Figure 6 (b) where ZB and WZ structures are indicated by light blue and red atoms respectively, and atoms that do not match either ZB or WZ are indicated in dark blue and are labeled "UD" for undetermined. This resulting CdTe SX film is used as a substrate for the growths of layered Cu/ZnTe in this section and also for the co-evaporated Cu and ZnTe growths in the following section.

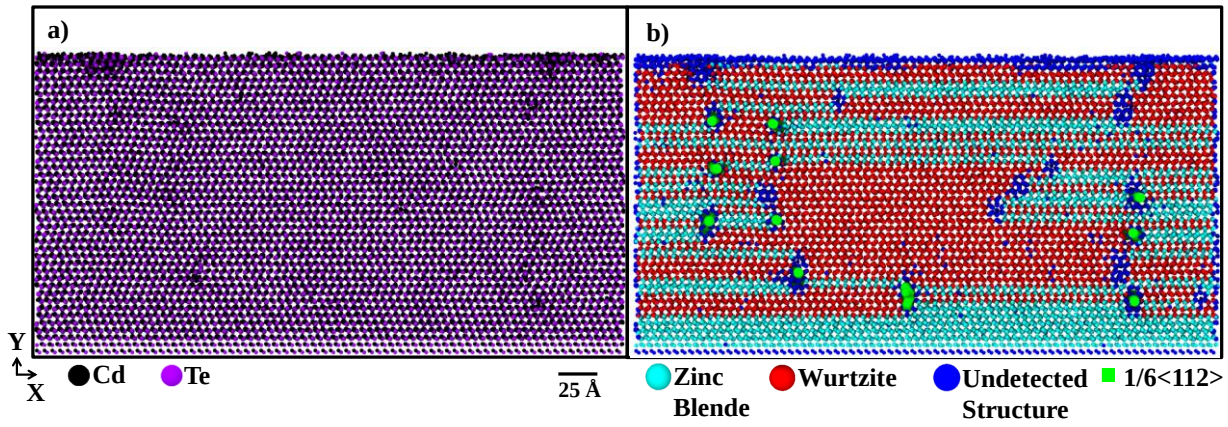

Figure 6: a) Atomic species map of the growth of CdTe on a perfect crystal CdTe and b) its structure and dislocation map.

4.1.2 ZnTe/Cu grown on SX CdTe Simulations

MD simulations were applied to simulate the growth of ZnTe/Cu on the CdTe single crystal substrates at Cu doses of 0.0, 0.3 and 8.0 monolayers (ML). Figure 7 (a) and (b) show cross-sectional views of the stack with 0.3ML of Cu before and after ZnTe, respectively. Figure 7 (c) is a plan view image showing the 0.3ML of Cu on the CdTe surface. Figure 7 (d) is a plan view slice at the interface between the ZnTe and CdTe where the 0.3ML copper is located. Similarly, Figure 8 (a) and (b) show cross-sectional views, and Figure 8 (c) and (d) show plan view images of the stack with 8.0ML of Cu, before and after deposition, respectively.

Time resolved analysis of the Cu deposition on CdTe showed a strong tendency for cluster formation even at doses as low as 0.3 ML. For example, Figure 7 (c) (which is a snap-shot after 0.3ML of deposition) shows the onset of Cu clustering. At early stages of deposition, Cu forms into small but highly mobile clusters. With the elapse of time, both the number and size of these clusters increase. Eventually the clusters merge resulting in a connected network with unfilled channels [56] as seen in Figure 8 c) and Figure 8 d) for the 8.0 ML of Cu

simulation. Once the network fully develops, no further Cu redistribution is observed and the unfilled regions remain.

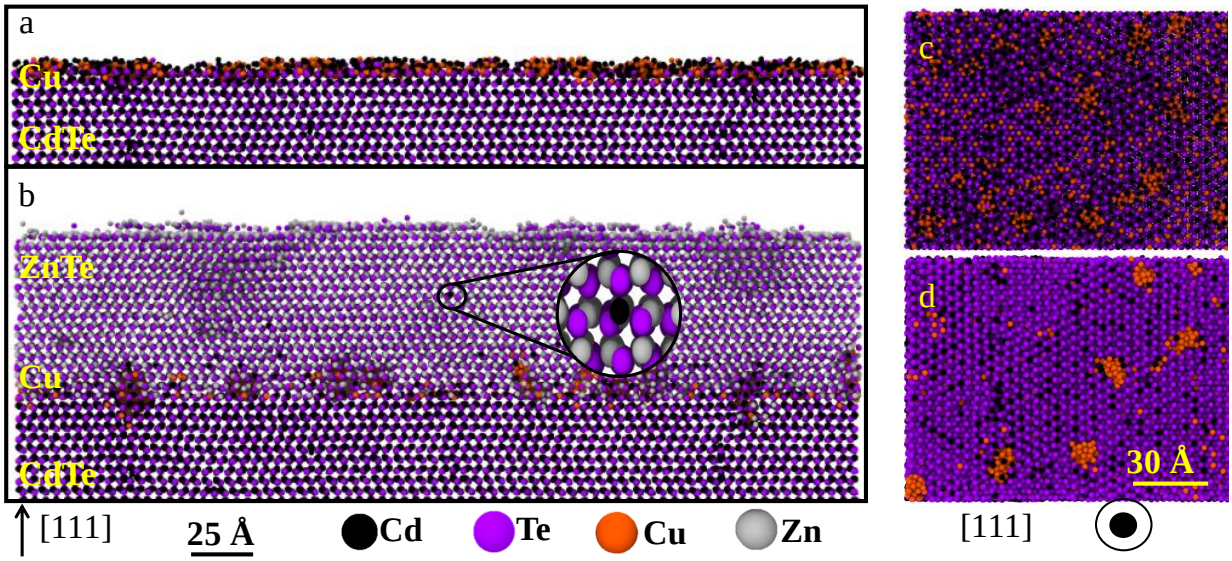

Figure 7: Cross-sectional views of a) 0.3ML-Cu/CdTe and b) ZnTe/0.3ML-Cu/CdTe, and plan-view images of c) 0.3ML-Cu/CdTe and d) ZnTe/0.3ML-Cu/CdTe.

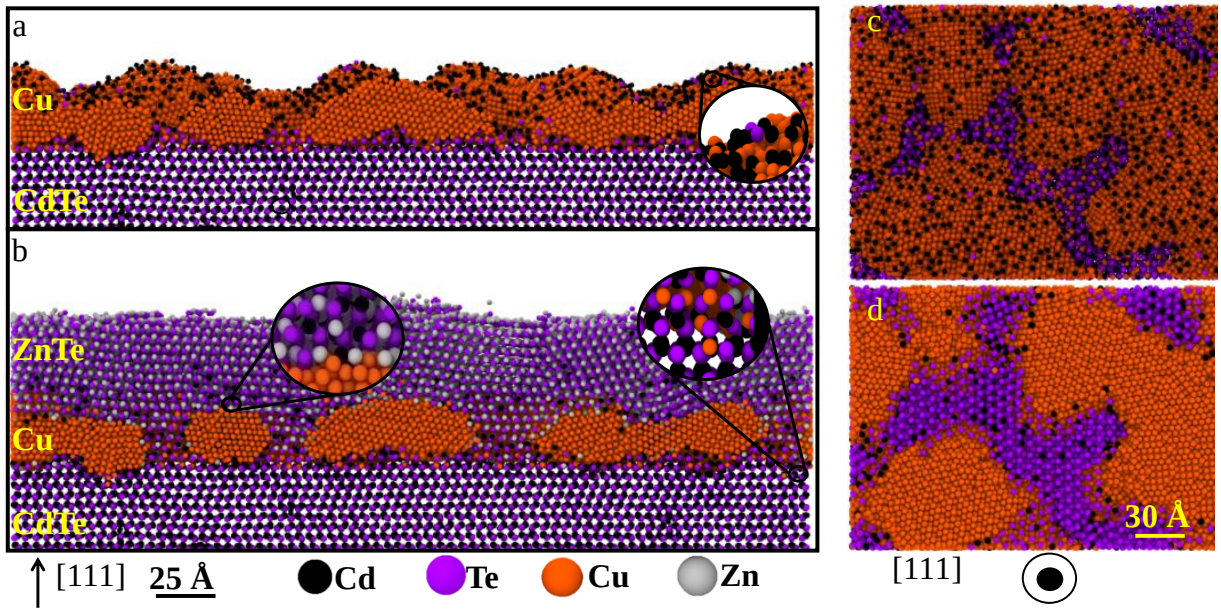

Figure 8: Cross-sectional views of a) 8.0ML-Cu/CdTe and b) ZnTe/8.0ML-Cu/CdTe, and plan-view images of c) 8.0ML-Cu/CdTe and d) ZnTe/8.0ML-Cu/CdTe.

The cluster nucleation, growth and coalescence behavior is supported by the graphs in Figure 9 (a) and (b) which tracked the number of Cu atoms within a single cluster over time for the 0.3 and 8.0 ML samples, respectively. At the start of Cu deposition, the Cu atoms are completely dissolved with no indication of clustering. However, after 1.5 ns and 2 ns of deposition, nucleation of Cu clusters is observed for the 0.3ML and 8.0 ML samples, respectively. Once nucleated, the Cu clusters grow with deposition time.

The sudden increase in cluster size indicated by the black arrows in Figure 9 (b) is due to coalescence of the cluster with another cluster. Notice that over time, there are approximately five clusters that join for the 8.0 ML simulation. In contrast, no cluster coalescence was observed in small cluster tracked in Figure 9 (a). This cluster is very small, mobile and grows slowly over the short period of time.

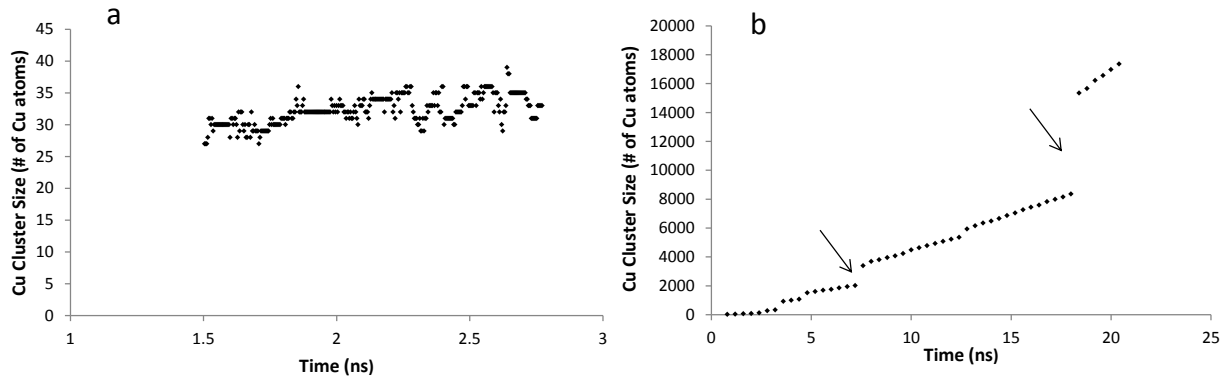

Figure 9: Cu cluster growth over time of the a) 0.3 ML and b) 8.0 ML Cu sample.

Significant diffusion of elemental Cd to the surface and incorporation into the ZnTe matrix is observed in Figure 8 (a) – (c) indicated by the uniformly distributed black dots in the ZnTe layers. Diffusion to the surface is in agreement with thermal desorption mass spectrometry studies in the literature [57] that show desorption of Cd atoms in proportion to Cu deposition on

CdTe. Since the only source of Cd is the CdTe layer, this means that the CdTe layer will be depleted of Cd. This is supported by the compositional analysis of the samples with 0.0, 0.3 and 8.0 of Cu as shown in Figure 10 (a)-(c), respectively. Comparison of the sample with 0.0 ML to those with 0.3 ML and 8.0 ML of Cu showed a depletion of Cd in the samples containing Cu. This effect is more pronounced in the sample with 8.0 ML of copper. This indicates that the presence of Cu enhances the displacement of Cd. Once ZnTe deposition starts, surface Cd atoms are incorporated into the ZnTe matrix as seen in the magnified insets in Figure 7 and Figure 8. This is corroborated by the long Cd tail in the ZnTe layer shown in Figure 10 (c). In contrast, Cu clusters are highly pure and do not incorporate Cd, Zn, or Te as seen on the Figure 7 and Figure 8. The results suggest that a mechanism for the incorporation of Cu, its diffusion and its role in doping the CdTe.

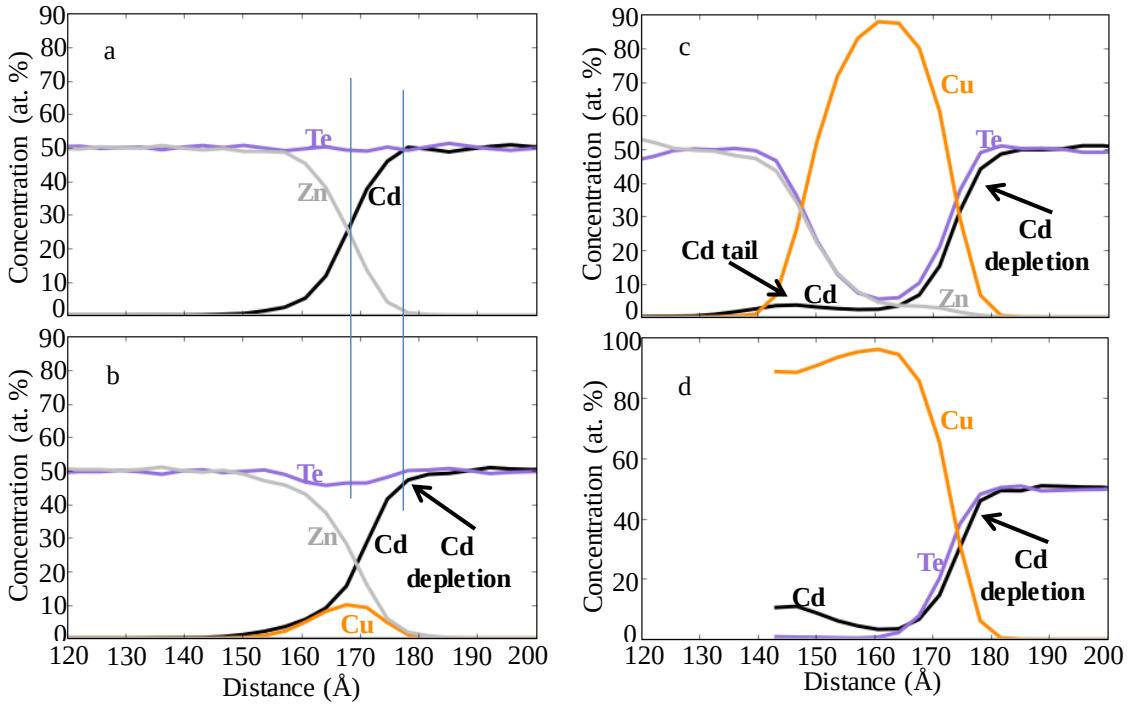

Figure 10: Composition profiles of a) ZnTe/CdTe, b) ZnTe/0.3ML-Cu/CdTe, c) ZnTe/8.0ML-Cu/CdTe and d) 8.0ML-Cu/CdTe.

4.1.3 Structural Analysis

To study the structure distribution of the film containing 0.3 ML, a structure map of the sample after growth was generated. The structure map is illustrated in Figure 11. Notice that the predominant structure in the epilayer is WZ. Due to the small size of the Cu clusters in this sample, it is hard to see their structure distribution by just looking at the figure. However, statistical data obtained from the analysis shows that the small Cu clusters were not part of any crystal structure. Dislocations are also illustrated in Figure 11 by the green lines. The only dislocation type found in this sample was Shockley partials. Notice that most of the dislocations are perpendicular to the growth plane, and therefore they look like green dots. Only few dislocations were found to orient differently and are located mostly at the interface.

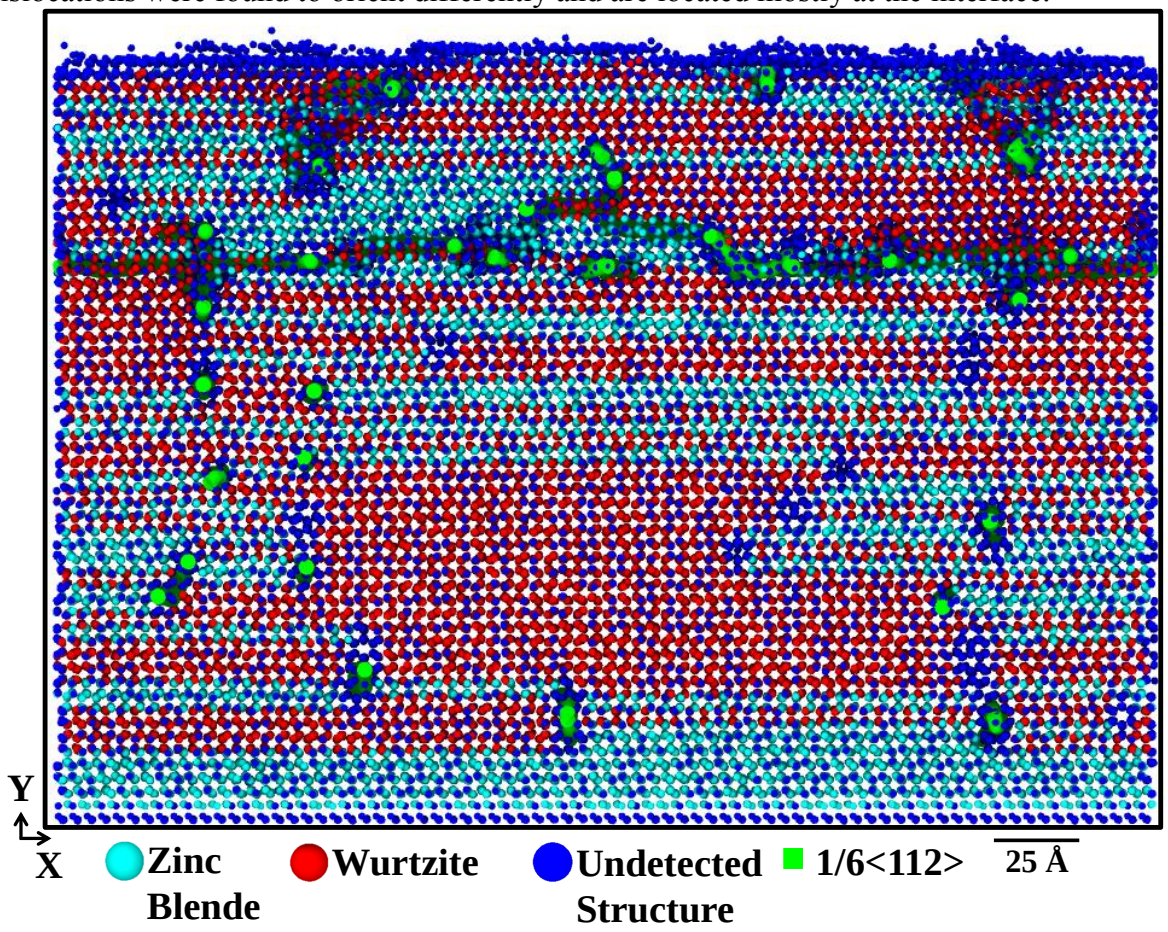

Figure 11: Structural and dislocation map of the sample containing 0.3 ML of Cu

Similar analysis was applied but now for the 8.0 ML sample. The result is shown in Figure 12. Notice that the structure map algorithm used (specified in the methodology) detects FCC and HCP (Figure 12(a)) separately from ZB and WZ (Figure 12(b)). Notice that Cu clusters in this sample are bigger and form part of FCC and HCP structures as seen in Figure 12(a). On the other hand, the predominant structure in the ZnTe layer is ZB as seen in Figure 12(b). This time, dislocations found were Frank partial, Shockley partial, and perfect dislocations. Most of the Shockley partial dislocations were located at the substrate while Frank partials and perfect dislocations were found in the ZnTe layer.

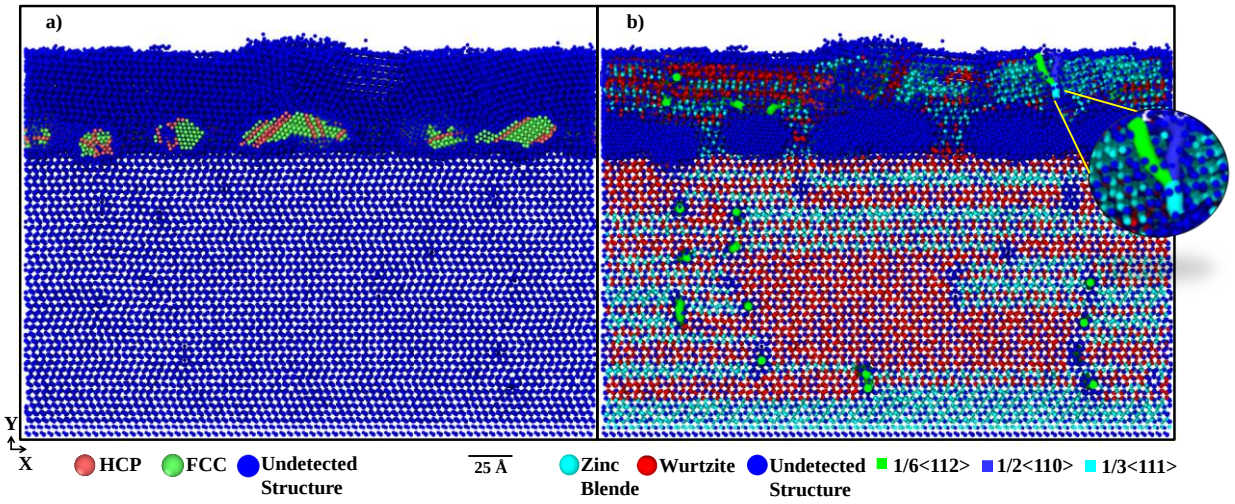

Figure 12: Structural and dislocation maps of the sample containing 8.0 ML of Cu. FCC and HCP detection is illustrated in a) while ZB and WZ detection is shown in b).

4.2 Growth of co-evaporated Cu and ZnTe on SX and PX CdTe

To replicate experimental conditions closely, simulations were performed where Cu and ZnTe were co-evaporated on CdTe. One set of growths was performed on a single-crystalline (SX) substrate and another on a polycrystalline substrate (PX). The SX substrate consisted of a perfect (111) CdTe single crystal of ~6 monolayers pre-deposited by a 150 Å CdTe film. Four sets of Cu:Zn:Te films were then deposited from vapor sources having flux ratios of (0:1:1), (2:9:9), (1:4:5) and (1:1:1) to study the effect of Cu loading. The 2:9:9 ratio was selected to

match the non-stoichiometric 10% experimental conditions from collaborators and that will be described in section 4.2.3. The 1:4:5 ratio which represents a stoichiometric 10% Cu loading was included for comparison with the non-stoichiometric case. These ratios are referred to as nominally 0%, 10%, stoichiometric 10% and 33%, respectively. The PX substrate consisted of a 120 Å polycrystalline CdS pre-deposited by a 100 Å CdTe film. Two sets of Cu:Zn:Te films were then deposited on the PX substrate having vapor flux ratios of 2:9:9 (10%) and 1:4:5 (stoichiometric 10%).

4.2.1 Atomic Species Maps

Cross-sectional atomic species maps of the resulting films from the simulated depositions on the monocrystalline and polycrystalline substrates are shown in Figure 13. Figure 13 (a)-(d) are films deposited with Cu loading of 0%, 10%, stoichiometric 10% and 33% on the monocrystalline substrate. The resulting copper content deposited was obtained by dividing the number of copper atoms fixed within a volume over the total number of atoms within the same volume (volume-averaged). The volume-averaged copper content in the epilayer films were 0%, 9.29%, 9.85%, and 33.35% in general agreement with the respective vapor fluxes. Figure 13 (e)-(f) are films deposited with Cu loading of 10% and stoichiometric 10% on the polycrystalline substrate. Similar to the monocrystalline case, the volume-averaged copper content in the films were 9.68% and 9.86%, in good agreement with the vapor fluxes. However, in contrast to the monocrystalline samples, the PX samples exhibited pronounced texturing and grain boundaries, consistent with the experimental results [58]. Moreover, the PX samples displayed larger interfacial and surface RMS roughness (5.4Å) in comparison to the SX samples (~1.4Å).

Figure 13 (b), (d) and (e) reveals the phenomenon of Cu clustering in the non-stoichiometric epilayers which is not the case for the stoichiometric epilayers. In general, the clusters are composed of pure Cu atoms and increase in size with Cu content.

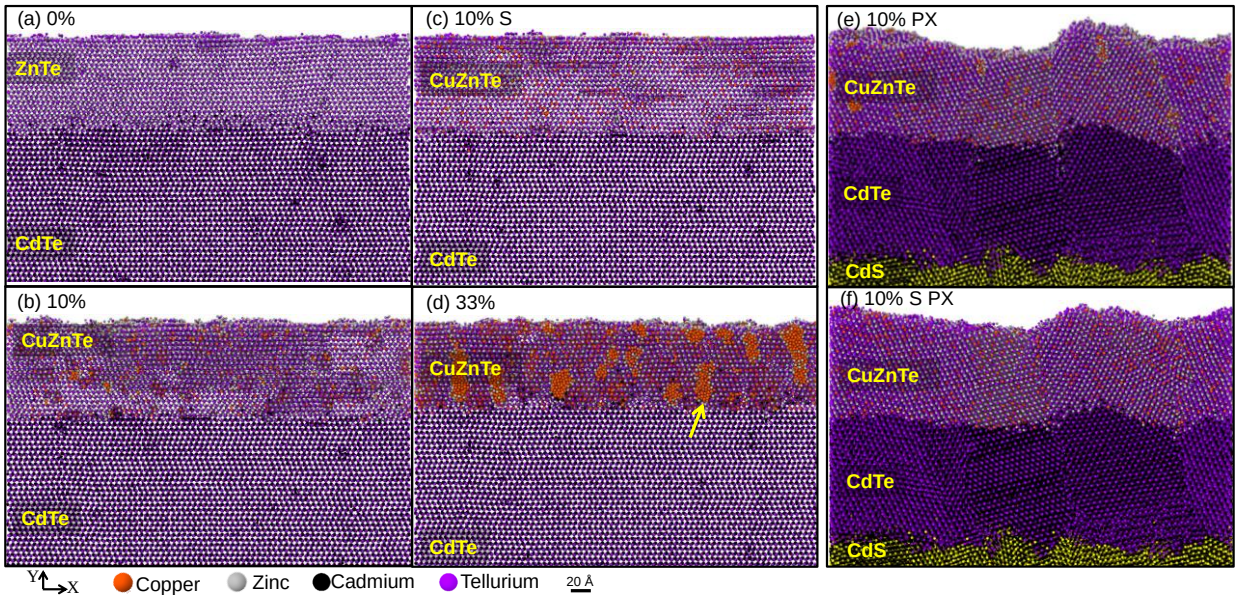

Figure 13: Cross-sectional images of simulated (Cu)ZnTe films grown on single crystalline CdTe with Cu loadings of (a) 0%, (b) 10%, (c) 33%, and (d) stoichiometric. Also, cross-sectional images of simulated (Cu)ZnTe films grown on polycrystalline CdTe with Cu loadings of (e) 10% Cu, and stoichiometric (f).

The cluster size increases with deposition time but reaches a plateau as seen in Figure 14. For example, two clusters in the 10% and 33% Cu SX samples were individually analyzed and observed to grow with time until maximum sizes of ~70 and 680 Cu atoms were reached, respectively. Cluster coalescence was also observed during growth as shown by the arrow in Figure 13 (d) pointing a dumbbell-shaped cluster formed by the coalescence of two neighboring clusters. This is confirmed by the sudden increase of Cu cluster size indicated by the black oval in Figure 14. In comparison to SX samples, the cluster growth over time in the 10% Cu PX

sample shows similar trend to that of the 10% Cu SX. However, it took more time for the cluster to reach a constant value.

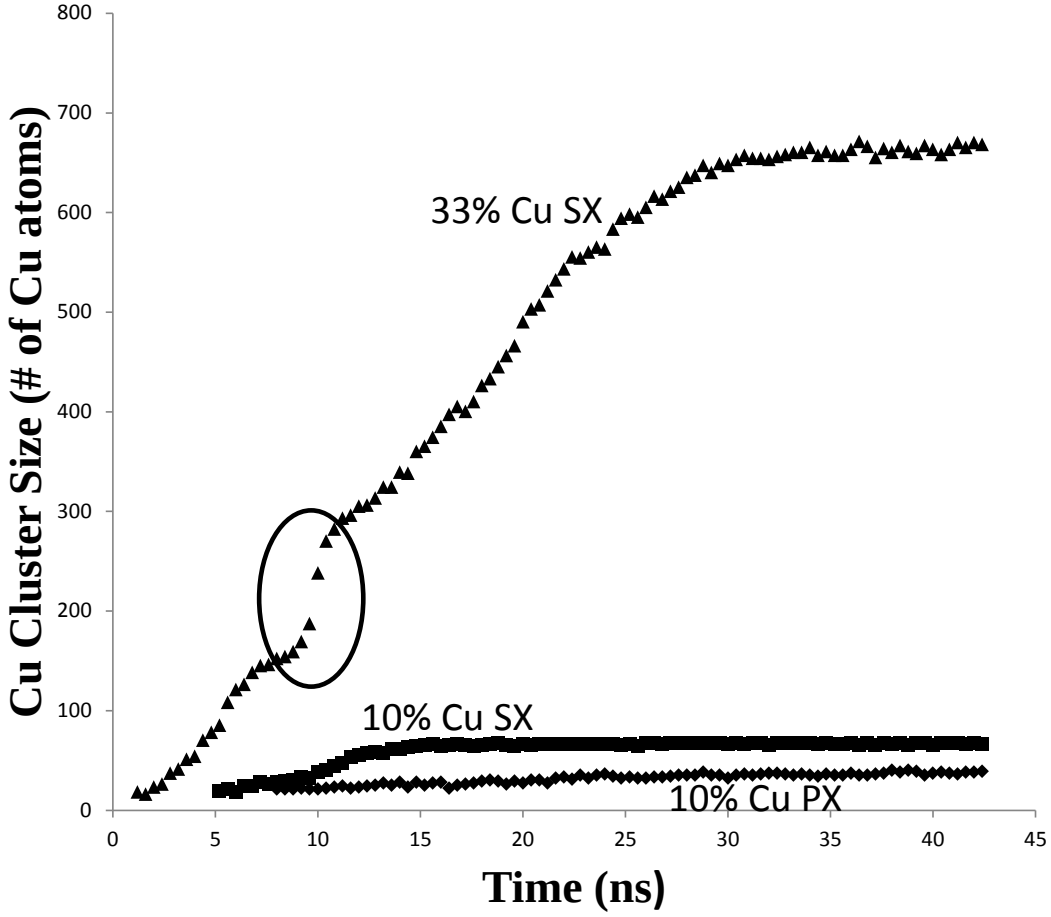

Figure 14: Cu cluster growth over time of the 10% Cu SX, 33% Cu SX, and 10% Cu PX samples

4.2.2 Structural Analysis

The deposited films exhibit polytypism where local regions vary from zincblende (ZB) and wurtize (WZ). Moreover, the films also exhibit amorphous regions. To explore this, structural maps of the configurations shown in Figure 13 (a) – (f) are reproduced in Figure 15 (a) – (f). Notice that UD atoms are mostly located in disordered regions associated with dislocations, grain boundaries, or surfaces. As observed in the literature, the predominant polytypes are WZ

and ZB [59]. The Cu clusters appear dark blue as indicated by the yellow ovals of Figure 15 (d) and (e). This is an indication that the Cu clusters are mostly amorphous. However, a small fraction of the larger clusters are seen to nucleate into FCC lattice after some time. Interestingly, the SX samples are predominantly WZ (Figure 15 (a) – (d)) while the PX samples are mainly ZB (Figure 15 (e) and (f)). The atoms at low-symmetry grain boundaries in Figure 15 (e) and (f) are also UD due to the high level of disorder. In the 33% SX sample, the Cu clusters bound stacking faults where otherwise Shockley partial dislocations might be located. In the 10% PX sample, the clusters form mainly at defected regions suggesting rejection of excess Cu atoms from the matrix to defected regions where they precipitate.

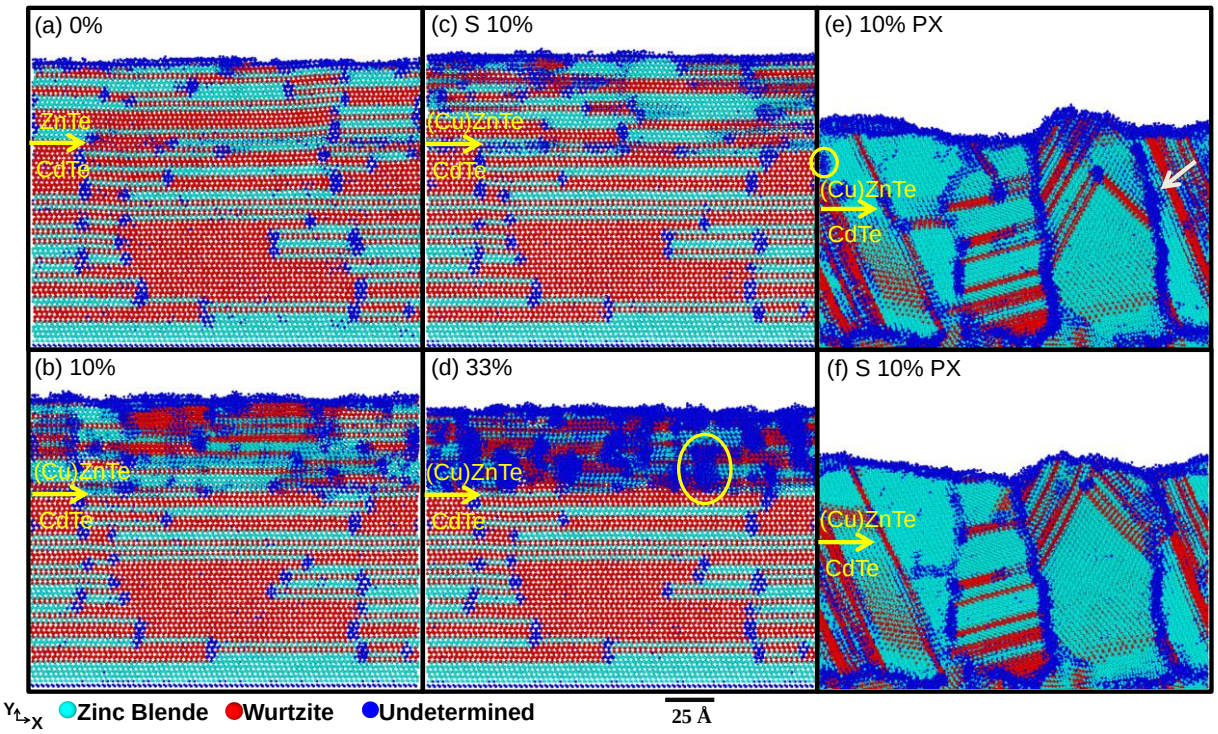

Figure 15: Structural maps of simulated (Cu)ZnTe films grown on single crystalline CdTe with Cu loadings of (a) 0%, (b) 10%, (c) stoichiometric 10% and (d) 33%. Also, cross-sectional images of simulated (Cu)ZnTe films grown on polycrystalline CdTe with Cu loadings of (e) 10% and (f) stoichiometric 10%.

Quantitatively, it is found that in the monocrystalline substrate 53% of the atoms are arranged in a WZ lattice, followed by 35% ZB, and 12% UD. The epilayer atoms in the 0% Cu

SX sample have the same proportion of polytypes as the CdTe layer, however there is a general trend for the atoms to nucleate more into the ZB lattice with increasing Cu loading. The proportion of UD atoms also increases with Cu loading. In fact, most of the atoms in the 33% SX epilayer are UD and is attributed to the relatively large Cu clusters and high defect density in the film. On the other hand, the 10% PX substrate and epilayer are mostly ZB (57%), followed by 22% UD, and 21% WZ.

It is instructive to study incorporation and diffusion of Zn and Cu in the substrates CdTe and Cd in the (Cu)ZnTe epilayers. Statistical analysis showed that Zn and Cu do not incorporate well into the lattices in the monocrystalline substrates. In other words, a disproportionately large number of Zn and Cu atoms are UD (between 18% and 46%) in the 0%, 10%, and 33% SX substrates. We speculate that those atoms diffuse through disordered regions such as dislocations and stacking faults but require more time to be substitutionally incorporated. In contrast, Zn and Cu atoms are incorporated more into the ZB and WZ structures in the stoichiometric SX sample. Similarly, Zn and Cu were incorporated in equal proportion to the ZB, WZ and UD structures in the polycrystalline sample.

Analysis showed that Cu atoms are incorporated into group II sub-lattice sites by displacing Cd atoms to form localized Cu_xTe. The displaced Cd atoms presumably then diffuse to the (Cu)ZnTe epilayer. Once in the epilayer, the Cd atoms are substitutionally incorporated well into both WZ and ZB lattices, especially in the polycrystalline sample.

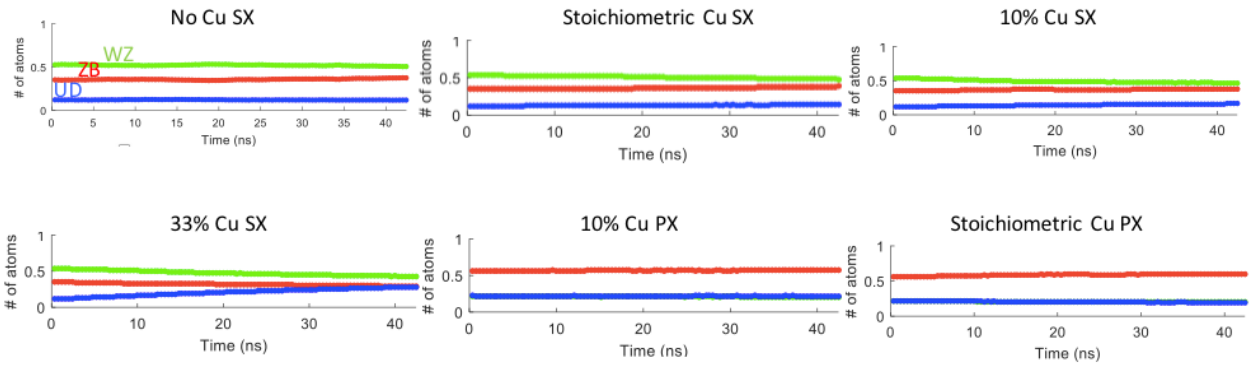

Figure 16: Structural time evolution of all atoms during ZnTe deposition on both substrate and grown layer.

Graphs in Figure 16 show the time evolution of the incorporation of all atoms in both the substrate and the epilayer in the WZ, ZB and UD structures. Red, green and blue represent the ZB, WZ and UD, respectively. All graphs show the time evolution up to 42.4 nanoseconds after (Cu)ZnTe deposition. It is highly noticeable and confirmed by the structural images on Figure 15, that the preferential crystal structure in the SX samples is WZ and the preferential crystal structure in the PX samples is ZB. However, the difference in percentage of ZB and WZ structures in PX is greater than it is in SX. Additionally, ZB structure increase over time and it almost reaches the same percentage from that of WZ. This suggests that if deposition is longer than 42.4 ns, ZB structure would either match WZ structure or overpass it. Also, we can see that in the 33% Cu SX sample, the atoms in the UD structure increase rapidly. This, as we saw before, is caused mainly due to the high concentration of clusters.

4.2.3 Experimental Corroboration

To validate our simulated results, experiments were carried out by Dr. Colin Wolden from Colorado School of Mines. The following data is directly quoted from his work in collaboration with our research group:

"Briefly, 1500 Å of CdS is deposited on commercial FTO–coated glass by evaporation. Next, ~4 microns of CdTe is deposited and subsequently exposed to vapor $CdCl_2$ treatment at 400 ^{o}C. Before back contact deposition the device is briefly dipped in a methanol/Br_2 mixture to

remove surface contaminants from the $CdCl_2$ treatment step. A ZnTe:Cu buffer layer is deposited by co-evaporating ZnTe and Cu at deposition ratios of ~5 Å/sec and ~0.5 Å/sec, respectively. Deposition time was ~5 min to obtain a total thickness of 1500 Å for ZnTe and 150 Å for Cu as measured by quartz crystal microbalance. The device structure was completed by evaporation of 1000 Å of gold, which served as the metallization layer. Device activation was achieved by rapid thermal process (RTP) for 30 sec at 320^{o}C. Posteriorly, an additional RTP process of 30 seconds at 330 ^{o}C was performed in order to study the impact of an extra thermal process.

Atom probe tomography (APT) analyses were performed on a Cameca LEAP 4000X Si local electrode atom probe instrument using parameters optimized for quantitative evaluation of these materials [60].Additionally, transmission electron microscopy (TEM) images before and after APT analyses were acquired with a Philips CM200 TEM using a holder specifically designed for imaging APT specimens [61]. High resolution TEM imaging was carried out in a FEI Tecnai F20 equipped with an Oxford Instruments X-Max 80 silicon drift detector (SDD) energy dispersive X-ray detector (EDX). EDX was used to produce chemical distribution maps of the cells as well as line scans and point analysis for quantitative elemental analysis. Dynamic Secondary Ion Mass Spectrometry (SIMS) was performed using an ION-TOF Model IV, and the copper density was quantified by normalizing the measured Cu/Te ratio to the copper content in the as-deposited sample which was quantified by APT.

Simulated results are consistent with Cu clustering observed in experimental samples using atomic probe tomography (APT) as shown in Figure 17 (a) and (b). In the APT images Cd is represented as black, Zn is grey, Cu is orange, and Te is excluded for clarity. Note that the images provided are just 2D representations of the full 3D reconstructions. A sharp ZnTe/CdTe interface is observed in all samples, demarked by the grey/black border. Significant heterogeneity in the copper distribution is observed in all samples as discussed below. Figure 17 (a) displays the results for the as-deposited sample. During co-evaporation, the intent was to deposit copper uniformly throughout the buffer layer sample, though some variations are

observed which is attributed to the challenges of the co-evaporation process. The volume-averaged copper content in the as-deposited buffer was 9.8 at. %.

Figure 17 (b) shows the APT reconstruction of a sample processed with an optimal rapid thermal process (RTP) treatment. In this case, APT reveals considerable segregation of copper toward both the Au and CdTe interfaces. After RTP, the Cu is concentrated in these aggregates, where the local concentration exceeds 50 at. %. These images suggest that copper redistribution within the ZnTe region is controlled primarily by thermodynamic parameters such as solubility and partition functions as opposed to Fickian diffusion. The high localized levels of Cu suggest the possibility of Cu_xTe formation, as the regions with elevated Cu content are well-correlated to displacement of Zn. This finding is perhaps not surprising given that the energy required to form a Cu_2Te molecule (formation energy) is close to zero [23]."

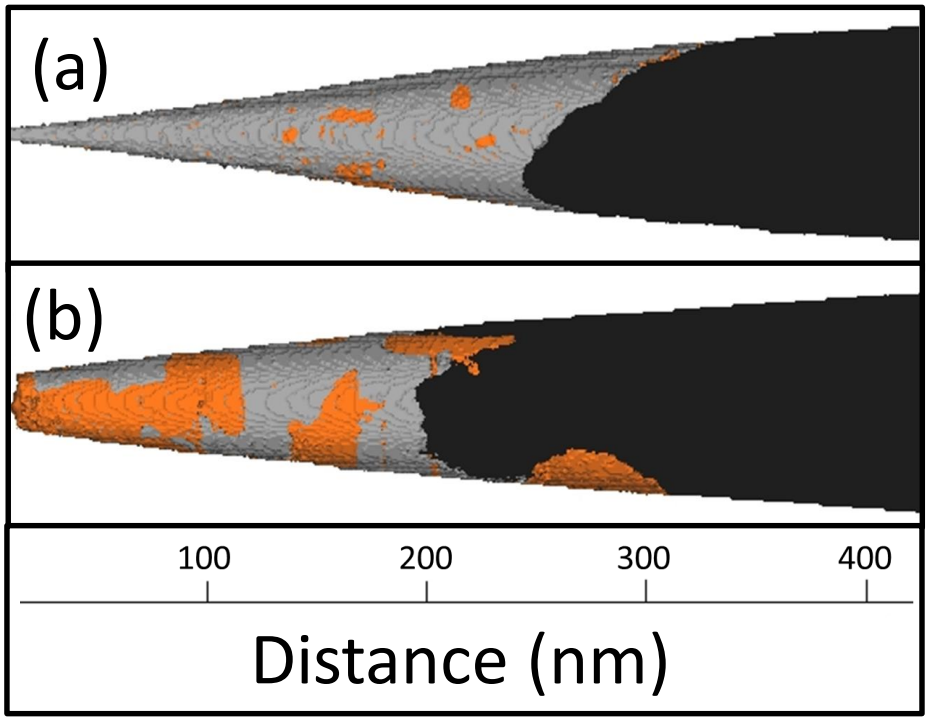

Figure 17: Atomic probe tomography of (Cu)ZnTe deposited on CdTe, (a) as deposited, and (b) after 30 sec anneal at ~873K. Cd, Zn, and Cu are colored black, grey, and orange respectively, and Te is excluded for clarity.

Notice that the sizes of the clusters in the sample with the RTP process are greater than those of the as-deposited sample. This suggests that the small clusters formed in the as-deposited sample coalescence to form bigger clusters during the RTP process. As seen from Figure 17, the average cluster size in the as-deposited sample is about 10 nm, where in the RTP process sample the average cluster size is around 100 nm. This is briefly 10 times greater than the as-deposited sample. Simulation wise, the increment on cluster size was also around 10 times greater. However, the simulations were not treated with the RTP process. Instead, the Cu loading was increased.

4.2.4 Predicted Composition Profiles and Diffusion

Inspection of Figure 13 suggested that there is significant diffusion of Cu and Zn into the CdTe substrates and Cd into the (Cu)ZnTe epilayers. To quantify this claim, composition profiles were constructured. Composition profiles of the samples with 0% Cu SX, 10% Cu SX, stoichiometric 10 % Cu SX, 33% Cu SX, 10% Cu PX, and stoichiometric 10% Cu PX are shown in Figure 18 (a) – (f), respectively.

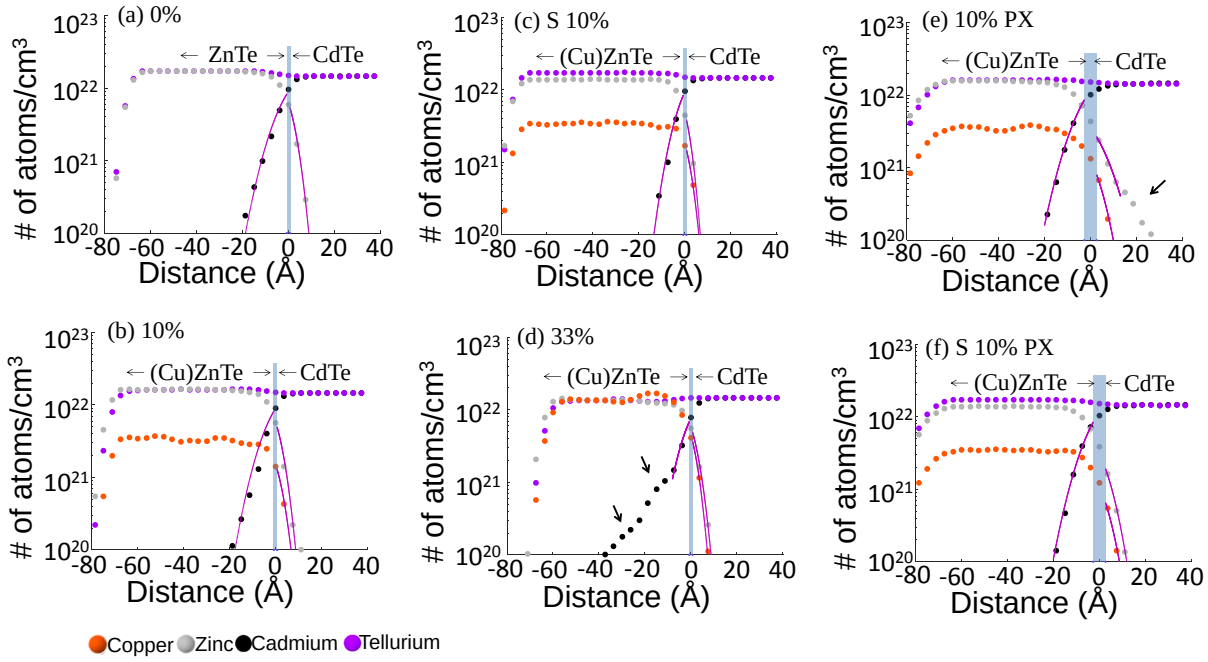

Figure 18: Composition profiles of simulated samples of (a) 0% SX, (b) 10% SX, (c) stoichiometric 10% SX, (d) 33% SX, (e) 10% PX and (f) stoichiometric 10% PX. The light blue bands correspond to regions of interfacial roughness.

Interface roughness is greater for the polycrystalline samples and it is illustrated in Figure 19. Root mean square roughness is measured to be 1.4 Å for the monocrystalline and 5.4 Å for polycrystalline. Color scale is blue to indicate low values of height of the surface and yellow to indicate high values. Certainly, the grain boundaries that terminate at the surface of the polycrystalline samples correspond to the blue regions in the 3D roughness representation.

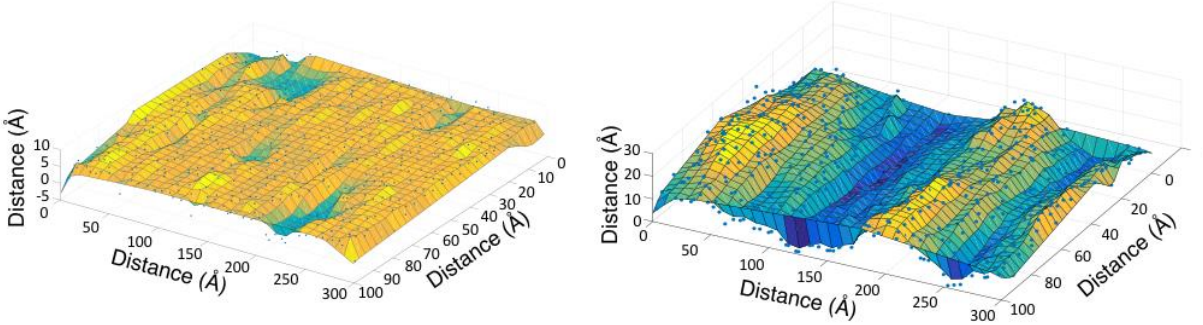

Figure 19: Surface roughness comparison between the (a) mono and (b) polycrystalline CdTe surface.

Given the diffusivities fitted from Figure 18 and the activation energies determined as specified in the methodology section 3.2, the pre-exponential coefficients were also determined. Results of the pre-exponential coefficients, and diffusivities obtained from Figure 18, are summarized in Table 1 for Cd, Zn, and Cu diffusion in the six samples 0% SX, 10% SX, stoichiometric 10% SX 33% SX, 10% PX and stoichiometric 10% PX. Note that the pre-exponential factors for Cd diffusion were not calculated because the activation energy for that element was not available.

Table 1: Diffusion coefficients and pre-exponential factors of Cd, Zn, and Cu in the SX samples.

	Cd in (Cu)ZnTe						Zn in CdTe						Cu in CdTe				
	SX				PX		SX				PX		SX			PX	
% Cu	0	10	33	Stoic.	10	Stoic.	0	10	33	Stoic.	10	Stoic.	10	33	Stoic.	10	Stoic.
D ($Å^2$/ps) ($X10^{-4}$)	6	6	4	4	8	7	2	2	2	4	8	4	2	1	1	4	3
D_0 ($Å^2$/ps) ($X10^4$)							3	3	3	6	12	6	35000	17000	17000	70000	52000

Table 1 indicates that the diffusion coefficients and pre-exponential factors for Zn and Cu diffusion are approximately the same in all the monocrystalline substrates, but they are larger in the polycrystalline substrate where a high degree of lattice disorder occurs including grain boundaries. This is consistent with the conventional understanding that diffusion is faster in disordered regions that often contain open areas.

Interestingly, the black arrows pointing at a wide Cd tail in the composition profile of 33% SX (Figure 18 (d)) sample show the presence of a higher diffusion coefficient. On closer inspection, the Cd wide tail starts at the position where the localized Cu concentration surpasses the nominal 33% suggesting Cu clustering in that region. Evidence from layered Cu and ZnTe simulation studies in the previous section show that Cd atoms surround the Cu clusters after Cu deposition at high Cu loadings. Subsequently, when ZnTe was deposited, some of the Cd atoms were then incorporated into the ZnTe matrix. Similarly, in the co-evaporated simulations, it is suspected that Cd is displaced by the higher degree of disorder created by Cu clusters and result in the long Cd tail. On the other hand, Cd diffusion in the polycrystalline epilayer was intuitively

lower than expected. However, given that Cd was very well incorporated in the polycrystalline epilayer and its degree of disorder is similar to the 10% SX epilayer including similar cluster size, these phenomena potentially mitigated its diffusion to be similar to the 10% SX epilayer.

4.2.5 Correlation with Experimental Diffusion

MD generated Cu diffusion parameters were compared to experimental results as seen in Table 2. The composition profiles and complementary error function fits of the simulation and experiment are shown in Figure 20. The complementary-error function was first fitted to the simulated data using only D_0 as the fitting parameter and obtained a good fit at D_0=70,000 $Å^2$/ps as shown in Table 2. This D_0 was then used in the experimental fits and moreover used the temperature as the fitting parameter. Surprisingly, good fits were obtained to both experimental profiles with a sole temperature value of 600 °C (873 K) although the fit is exponentially sensitive to temperature. However the predicted temperature of 600 °C (873 K) is higher than the experimental set point of 320 °C. It is speculated that the actual temperature of the ZnTe layer was much higher than the set point (close to 600 °C). This is supported by the fact that in separate experiments, set points higher than 320 °C yielded significant sublimation of the CdTe films which occurs at temperatures close to 600 °C for this material.

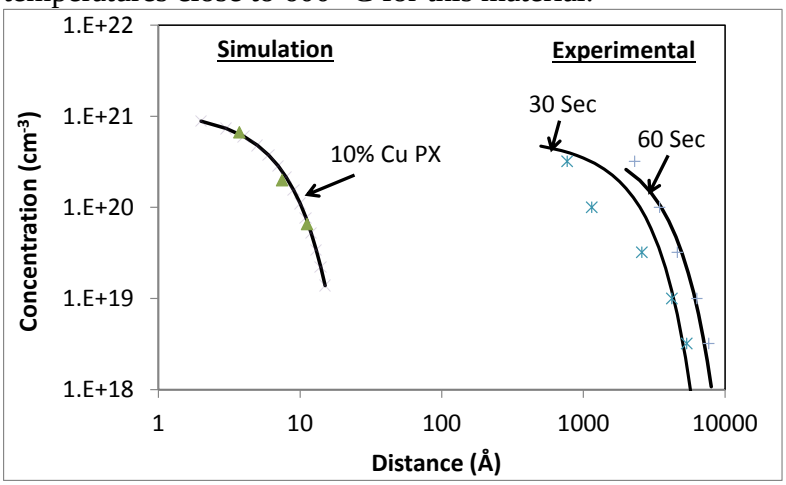

Figure 20: Direct comparison between the composition profiles of simulation and experimental samples.

Table 2: The growth conditions, and the fitted parameters for Cu diffusion into CdTe, for simulation and experiment.

	Simulation	Experiment	
	10% PX	OPT	OVH
Temperature (K)	1150	873	873
Time (ps)	42400	$3x10^{13}$	$6x10^{13}$
Q (eV)	2.79	2.79	2.79
Peak conc. (cm^{-3})	$1.2x10^{21}$	$6x10^{20}$	$6x10^{20}$
D ($Å^2$/ps)(10^{-4})	4	$5.47x10^{-4}$	$5.47x10^{-4}$
D_0 ($Å^2$/ps)(10^4)	70000	70000	70000

4.2.6 Localized Diffusion Analysis – Effect of Defects on Diffusion

To examine the local effect of defects on diffusion, elemental maps were constructed where only one element is shown at a time in the configuration. The elemental maps obtained from simulation and EDS experiment are compared in Figure 21 for the 10% Cu PX sample. The EDS profiles were obtained from a TEM cross section that contained two large CdTe grains that meet at the vertex of the ZnTe/CdTe interface (white line), with their boundary running vertically from that point. The grain on the right was pristine while the grain on the left contains a defect adjacent to the interface. The defect is deficient in Cd and preferentially enriched in Cu, Te, and Zn. Inter-diffusion of Cu, Cd and Zn atoms can be seen in both experimental and simulated mappings. The simulation results shown in Figure 21 (a) reveal that most diffusion occurred through the grain boundary (labeled as GB), some diffusion also proceeded through the stacking fault (labeled as SF), but no diffusion can be found in the regions with no defects (labeled as SX). These theoretical predictions are in good qualitative agreement with the experimental images shown in Figure 21 (b), where inter-diffusion is pronounced at the defect and along the grain boundary.

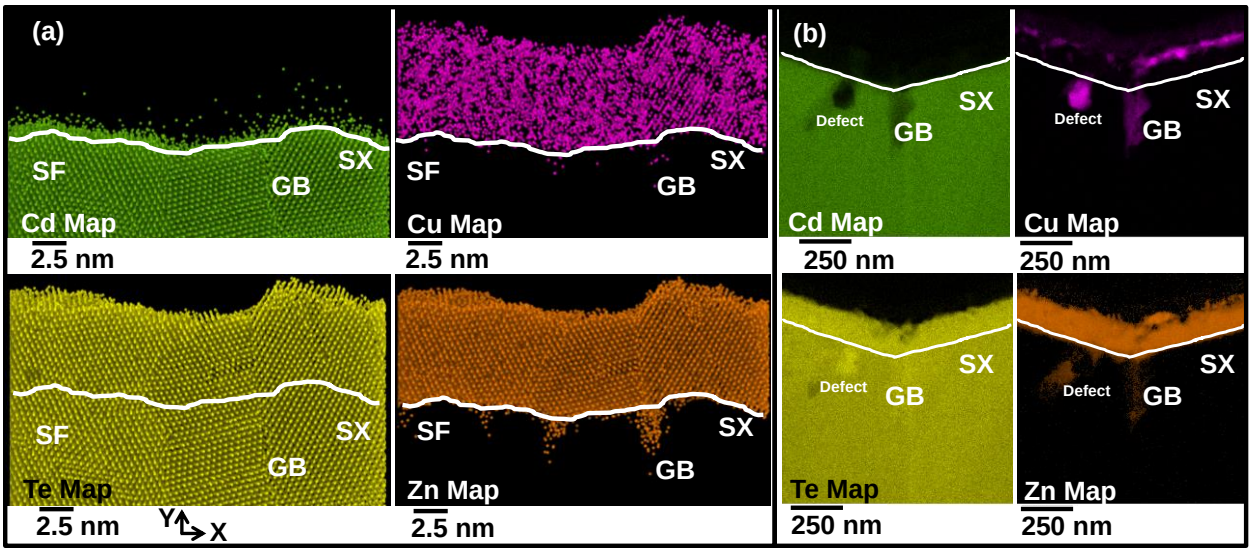

Figure 21: Comparison of elemental maps of the 10% PX interface between (a) simulation and (b) experiment.

Localized Cu compositional profiles were computed of the regions that were highly crystalline, contained the stacking fault, and contained the grain boundary in the 10% PX simulated sample as shown on Figure 22. Complementary-error functions were fitted to the data to obtain D and D_0 and are listed in Table 3. As anticipated, diffusion was fastest through the grain boundary presumably due to the higher degree of disorder in that region. This was followed by the stacking fault which had higher diffusion compared to the highly perfect area.

In the previous section, the pre-exponential factors in PX samples were higher compared to the SX samples since defect concentration leads to a higher available space for atoms to travel. This is corroborated by diffusion profiles of Cu at the three regions of the 10% PX sample. Notice that the pre-exponential factor increases as the defect density increases.

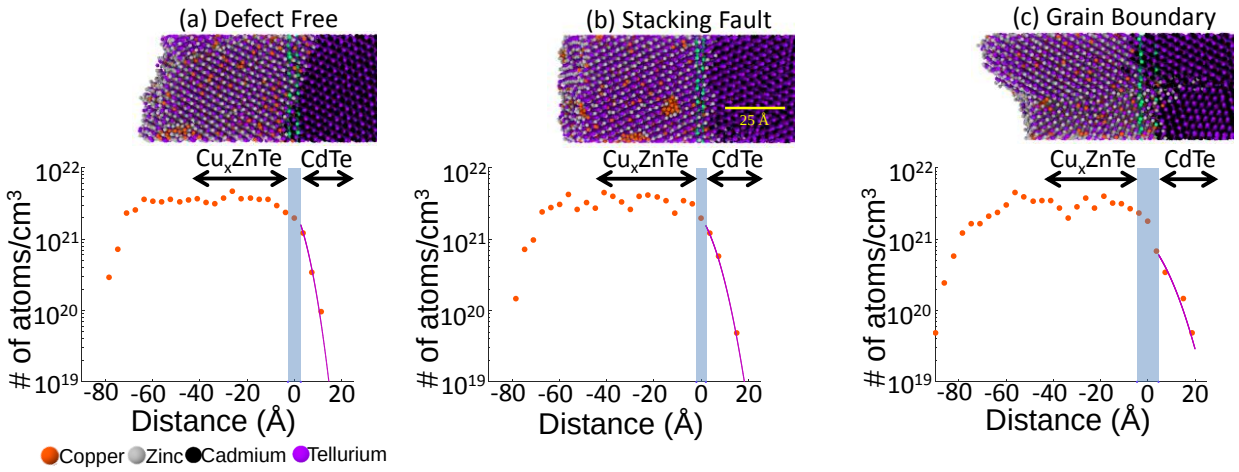

Figure 22: Cu composition profiles of the regions containing a) continuous layer, b) stacking fault, and (c) a grain boundary.

Table 3: Pre-exponential factor and diffusivity of three regions in the polycrystalline sample.

	SX	SF	GB
D ($Å^2$/ps) ($x10^{-4}$)	3	5	10
D_0 ($Å^2$/ps) ($x10^4$)	50000	90000	180000

4.2.7 Dislocation Density Analysis

Numerous stacking faults are present in all the monocrystalline samples oriented along the <111> close-packed planes and are parallel to the growth plane. These stacking faults are bounded by 1/6<112> Shockley partial dislocations as indicated by small gray regions as seen in Figure 23(a) – (d). Notice that this time we are using gray color for the UD atoms in order to have a better color contrast with the dislocations. Also, Shockley partial dislocations are also observed along the interface between (Cu)ZnTe and CdTe presumably to accommodate the lattice mismatch between the two materials. In contrast, the stacking faults in the polycrystalline samples are oriented in various directions mirroring texturing of the film and are mainly bounded by grain boundaries. The grain boundaries are indicated by amorphous lines.

The dislocation density in the ZnTe layer of the 0% SX sample is similar to the CdTe substrate. However, in the samples with 10% and 33% Cu, the number of dislocations increases with Cu content. Surprisingly, in the stoichiometric Cu sample, the dislocation density is similar

than that of 10% and 33% Cu samples. The dislocations clearly delineate between the (Cu)ZnTe and CdTe layers. In contrast, the delineation between the layers is not so clear in the PX samples. In this case, the dislocation types are more varied and spatially uniform with no clear distinction between the (Cu)ZnTe and CdTe layers. Also, dislocation density is less in the stoichiometric Cu PX sample than in the 10% Cu sample.

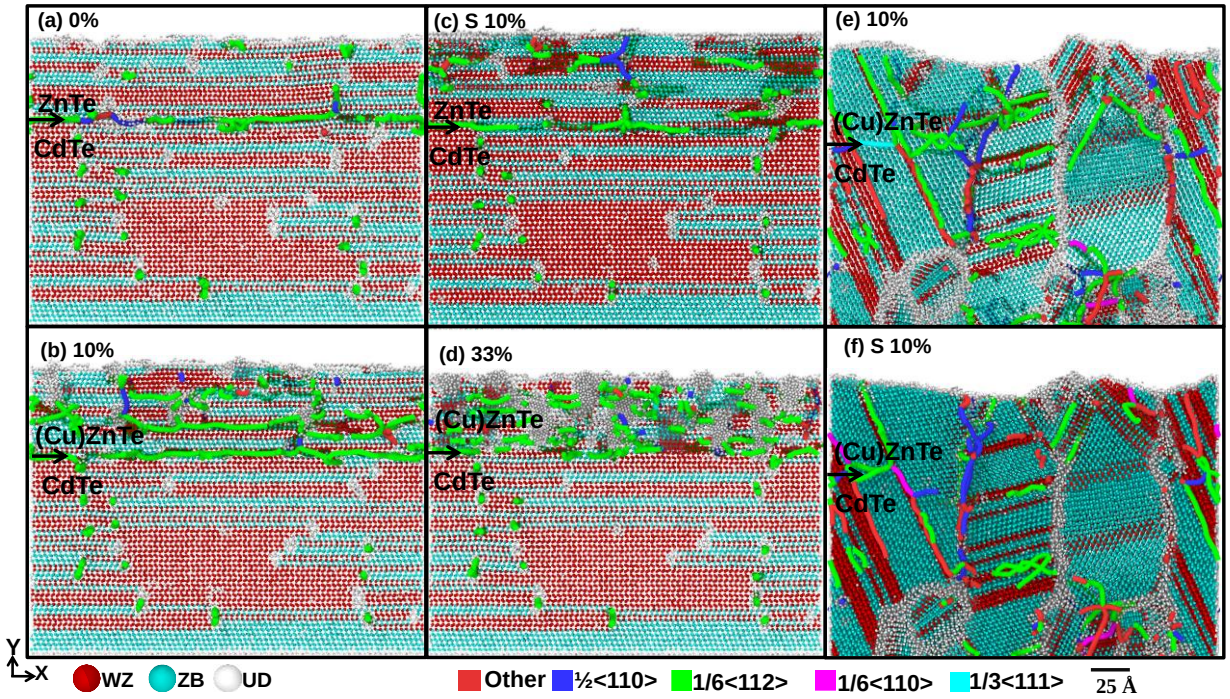

Figure 23: Dislocation maps of simulated (Cu)ZnTe films grown on single crystalline CdTe with Cu loadings of (a) 0%, (b) 10%, (c) stoichiometric 10% and (d) 33%. Also, dislocation maps of simulated (Cu)ZnTe films grown on polycrystalline CdTe with Cu loadings of (e) 10% and (f) stoichiometric 10%.

4.3 Polycrystalline growth simulation using MD

Polycrystalline growths shown in the previous sections are the result of growing on top of an amorphous CdS substrate. Importantly, this is the first time that MD simulations predict polycrystalline phenomena for CdTe heterojunctions. The methodology to accomplish these growths will be described in section 4.3.1. CdS morphology and first stages of polycrystalline growth will be described in section 4.3.2. Interesting phenomena such as grain boundary migration in CdTe was observed and will be described in section 4.3.3. Finally, the overall structure (Cu)ZnTe/CdTe/CdS will be presented in section 4.3.4.

4.3.1 Amorphous substrate preparation

The amorphous substrate used for the polycrystalline growths was created based in a single crystal zinc blende structure of ~55 Å thick. Two fixed regions and one thermal region were defined in the single crystal structure as seen in Figure 24 (a). Fixed regions were defined using the set velocity command in the LAMMPS code while thermal region was created using the create velocity command and the NVT canonical ensemble. Thermal region was heat treated with a temperature of ~2250 K for ~40 ps. After the treatment, temperature was linearly decreased to 0 K for an additional 20 ps as seen in Figure 24 (c). After anneal, the sample resulted in an amorphous region located between two fixed regions as illustrated in Figure 24 (b). The resulting structure was sliced to a thickness of ~30 Å to use as a substrate for deposition as seen in Figure 24 (d). The substrate shows a high degree of disorder and it is confirmed by the structural identification algorithm which shows 100% UD structures.

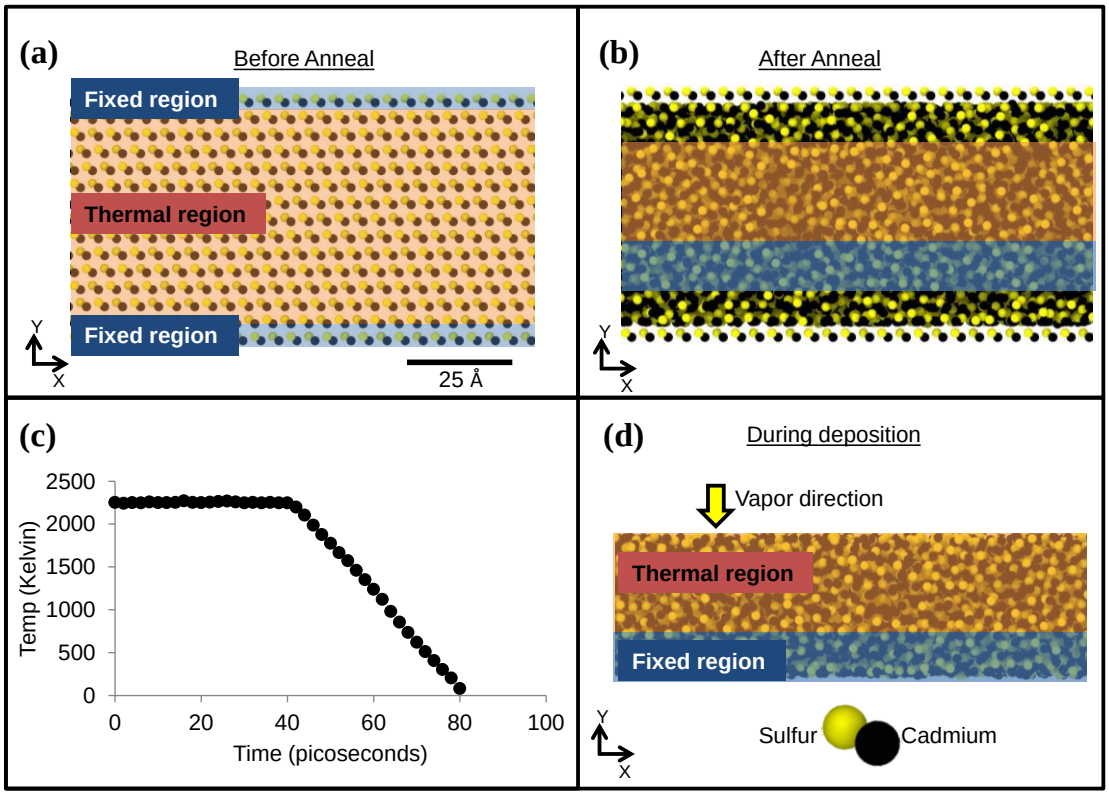

Figure 24: Visual explanation of amorphous substrate construction (a) before anneal, (b) after anneal, (c) temperature profile, and (d) during deposition.

4.3.2 Polycrystalline CdS Growth

In our effort to reproduce polycrystalline film growth, the amorphous layer created was used as a substrate for CdS deposition. Our original guess was that Cd and S atoms would nucleate randomly due to the randomness of the amorphous substrate and eventually form random crystallized regions. These regions would grow and meet each other forming grain boundaries. Our results show nothing far from the original guess except that recrystallization of the amorphous substrate occurs simultaneously. For example, Figure 25 (a), (b) and (c) show the stages of CdS growth at 0, 3.2, and 48.4 nanoseconds (ns), respectively. Only a slice of the sample is showing in these figures. At 3.2 ns, CdS starts to recrystallize into WZ and ZB structures and, at the same time, more Cd and S atoms nucleate on top. These regions grow vertically over time forming columnar grains as shown by the small yellow arrow in Figure 25 (c). Grain boundaries also grow vertically as more atoms are incorporated as seen in the black arrows of Figure 25 (c). Polytypism is also observed as the film grows showing a preferential ZB structure, similar to the growth of SX CdTe in section 4.1. However, this time, wurtzite regions grow either diagonally or horizontally and in different directions as indicated by the thin yellow arrow in Figure 25 (c).

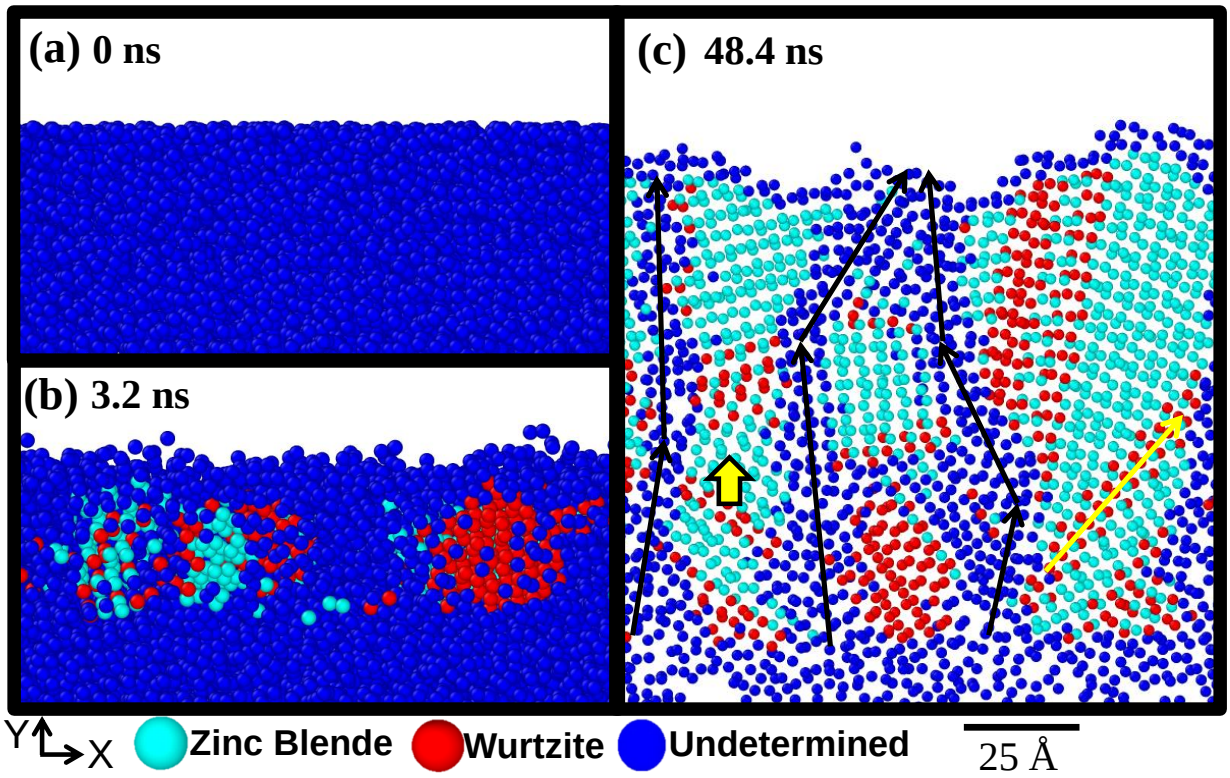

Figure 25: Timeframes of CdS deposition on top of the amorphous substrate at (a) 0, (b) 3.2, and (c) 48.4 ns.

The complete growth after 48.4 ns is shown in Figure 26. The growth was examined over the Z axis to confirm consistency of the columnar grains and polytypes. Surprisingly, the grains extend with similar morphology throughout the entire sample with the exception of small variations at grain boundary orientation. No grain boundary migration was observed over time of growth. However, the formation of new grains during growth was observed as indicated by the yellow arrow in Figure 26. Simulations of the growth of polycrystalline CdTe in section 4.2.4 and section 4.3.3 use the film in Figure 26 as a substrate.

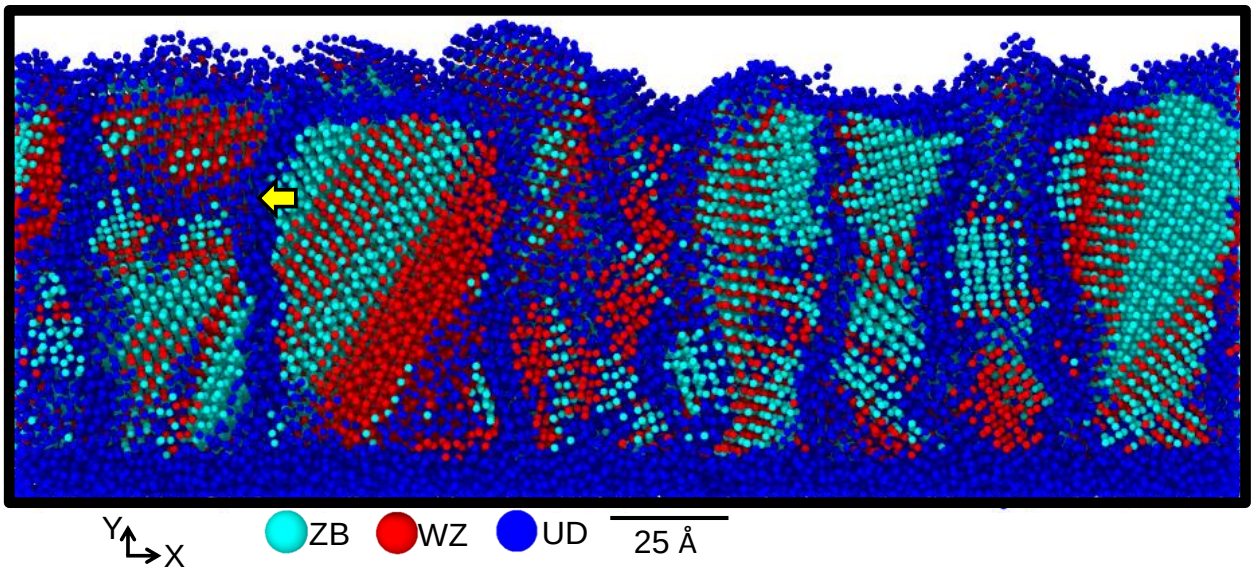

Figure 26: Final deposition of CdS on amorphous CdS substrate after 48.4 ns.

To compare the surface morphology of the polycrystalline CdTe and the polycrystalline CdS, surface roughness of the CdS film in Figure 26 was constructed and is depicted in Figure 27. Briefly, the surface morphology of the CdS does not have a direct impact on the morphology of the polycrystalline CdTe

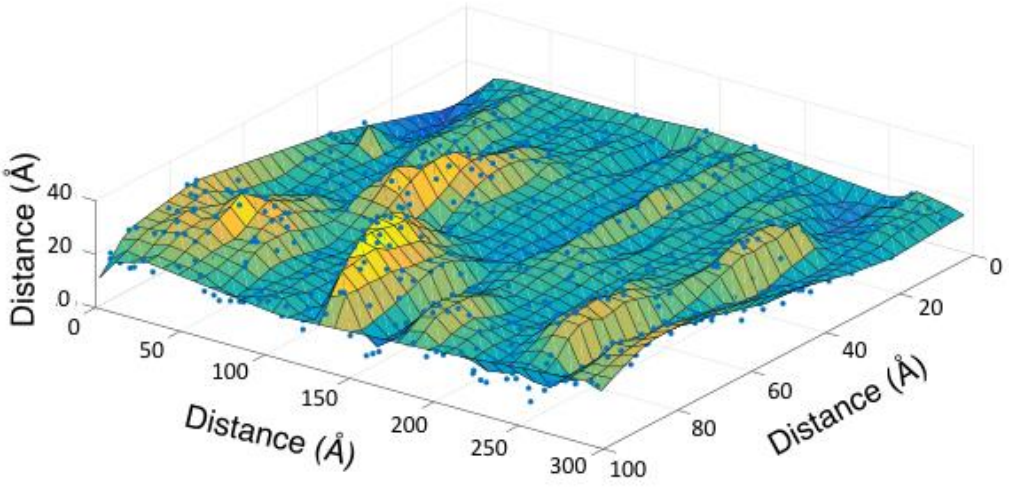

Figure 27: Surface roughness construction of the CdS surface after deposition.

It would be computationally expensive to reproduce polycrystalline films with similar thicknesses to those found experimentally. This is the main reason why we use much smaller sizes for our depositions. Nevertheless, the CdS experimental thickness used for the fabrication of solar cells ranges from 60 nm to 120 nm which is within range of MD simulation. Motivated by this fact, the continuation of the growth of CdS presented in Figure 26 is shown in Figure 28. An additional time of 95.2 ns was performed resulting in a total deposition time of 143.6 ns. A total thickness of 26.5 nm was accomplished. The atomic species map, structure map and dislocation map of this simulation are illustrated in Figure 28 (a), (b) and (c), respectively.

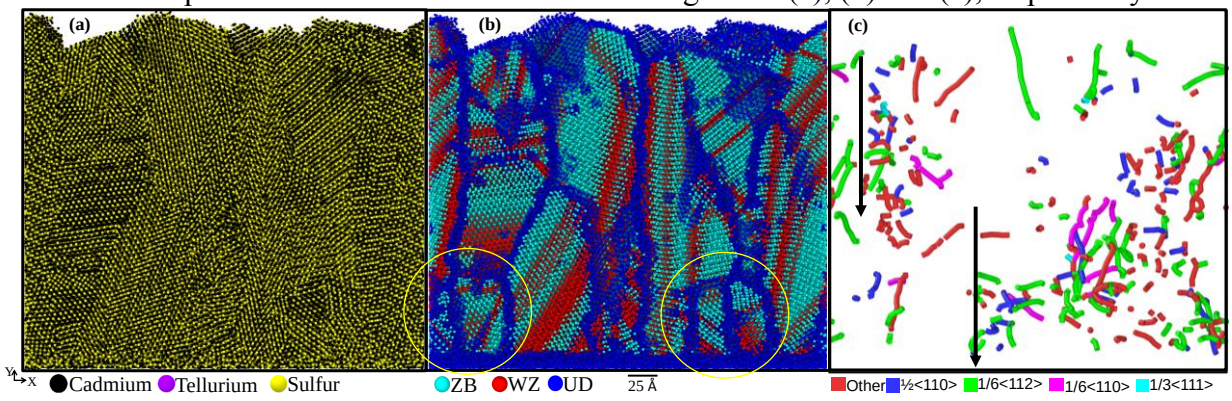

Figure 28: a) Atomistic visualization, b) structural map, and c) dislocation map of the CdS growth after an additional deposition time of 95.2 ns.

Generally, columnar grains with predominant ZB structure and few WZ regions were observed. Only few grains maintained their original morphology from the substrate as indicated by the circles in Figure 28 (b). Dislocation analysis in Figure 28 (c) show that dislocations form randomly and do not necessarily form part of a grain boundary. Grain boundaries are represented as black arrows in Figure 28 (c). Dislocation types found were perfect dislocations ½<110>, Shockley partial dislocations 1/6<112>, stair-rod dislocations 1/6<110>, and Frank partial dislocations 1/3<111>.

4.3.3 Polycrystalline (PX) CdTe Growth (Grain boundary migration)

CdTe was deposited on top of the resulting CdS polycrystal shown in Figure 26 to closely reproduce experiments. Time evolution of this growth between over the span of 4ns (24.4 and 28.4 ns) is shown in Figure 29. Within this time frame, grain boundary migration was observed. To a large degree, the CdTe layer mimics the crystal type and orientation of CdS including grain boundaries. The first frame at 24.4 ns shows a relatively large grain boundary in the CdTe in the shape of a "V" as indicated by the circle. However in the next frame (25.4 ns), some of the material within the V-boundary appears to have nucleated into a WZ phase. With continued deposition, the WZ phase grows in size causing its right grain boundary to move in a manner so as to lie at the CdTe/CdS interface. Within 4 ns the grain boundary becomes pinned at the interface between the CdTe and CdS presumably to release strain due to lattice mismatch and remains relatively immobile thereafter. The velocity of the grain boundary is ~0.009 Å/ps which is 4× the growth rate of the film.

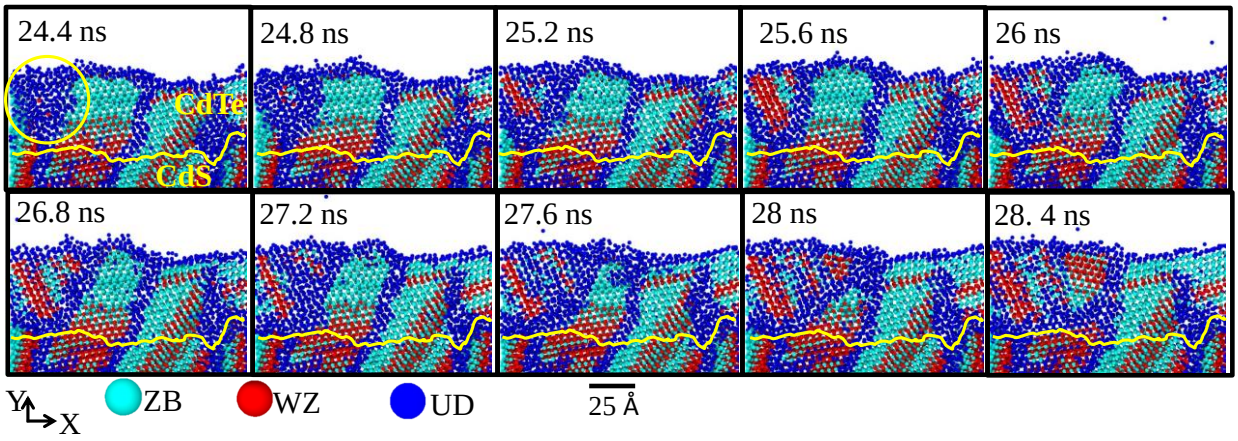

Figure 29: Structural map time evolution of the growth of CdTe on top of CdS between 24.4 ns and 28.4 ns.

Atomistic visualization and structure map of the complete growth after 46.8 ns of PX CdTe on PX CdS is shown in Figure 30 (a) and (b), respectively. Atomistic visualization shows how S atoms (yellow atoms) diffuse into the CdTe layer. CdTe grains are about two times

greater than the size of the CdS grains. Also, the predominant structure type is ZB with only a few WZ regions. A high proportion of the CdTe/CdS interface (indicated by the yellow line in Figure 30 (b)) is composed of disordered grain boundaries. However, a small region of continuous film between CdS and CdTe is observed indicating some degree of heteroepitaxy.

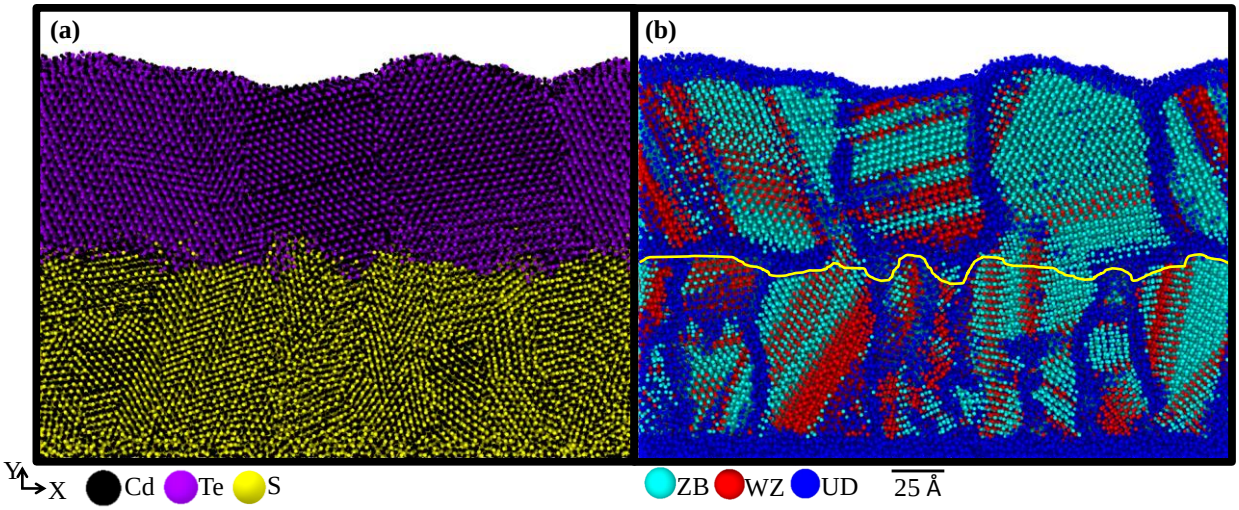

Figure 30: a) Atomistic visualization of the complete growth of CdTe on CdS and b) its structural map.

Further growth of the CdTe on the CdS results in grain growth and reduction of defect density within the growing CdTe in general agreement with experimental results. However, grain size and dislocation density in the underlying CdS remained relatively constant. Figure 31 shows the thicker CdTe/CdS structure after an additional 17.6 ns of deposition which yielded 37 Å more of CdTe thickness. Overall, the sizes of the grains increase with layer thickness throughout the CdTe/CdS stack resulting from the coalescence of grains and differential growth rates along different crystal orientations and/or defected areas. For example in Figure 31 (a), the grain boundaries marked “1” and “2” are expected to merge into one with continued growth allowing grains marked “A” and “C” to grow at the expense of grain “B”. Evidence of faster growth rate in defected regions is provided by the peak in the CdTe thickness which coincides with the 3 WZ stripes (indicating the presence of stacking faults) circled in Figure 31 (a). The difference in

growth rates also explains the relatively larger surface roughness of the polycrystalline films compared to the single crystal layers. Based on these findings, it is expected that the grain size will continue to increase with deposition.

Both the number of grain boundaries and dislocations decrease with continued CdTe deposition. Figure 31 (a) shows that the grains near the growth surface have fewer grain boundaries and stacking faults. Moreover, Figure 31 (b) shows that the number of dislocations decrease although their length increase with film height. Generally, the dislocations types found in the CdTe growth are perfect dislocations, Shockley partials, Frank partials, and other type of dislocations not detected by the dislocation algorithm. These "other" dislocations were extended across the (Cu)ZnTe/CdTe interface as indicated by the green circle in Figure 31 (b). Perfect dislocations are located along grain boundary 1 as indicated by the black circle in Figure 31 (b).

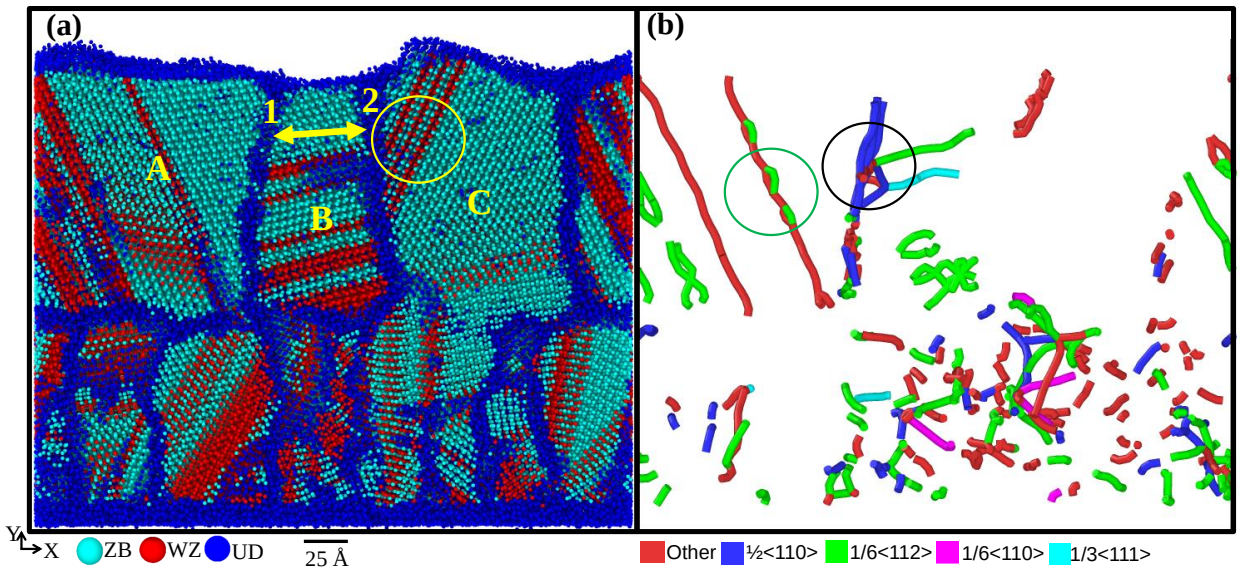

Figure 31: a) Structural and b) dislocation map of the additional growth of CdTe.

It is intriguing the way that dislocation networks form at grain boundaries. Since only one grain boundary in Figure 31 contained a dislocation network, it was suggested to look at the predominant atoms on both grain boundaries. Moreover, an algorithm was design to count the number of Te-Te error bonds across the grain boundaries and was applied to a slice containing

grain B and its grain boundaries (1 and 2) from Figure 31 (a) and illustrated in Figure 32 (a) and (b). Briefly, the number of Te-Te error bonds is greater in grain boundary 2 which did not contain dislocation networks.

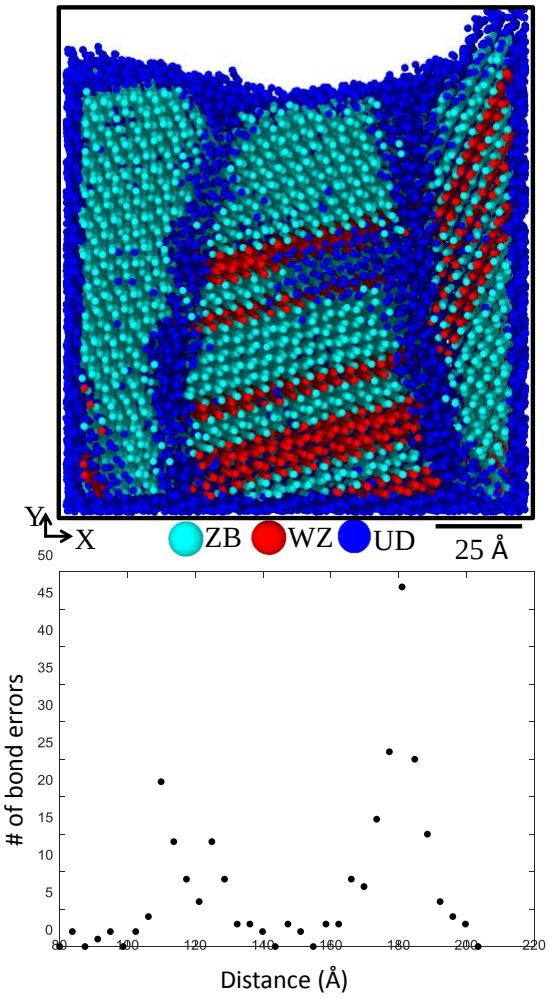

Figure 32: Analysis of the Te-Te error bond over distance.

4.3.4 Polycrystalline (PX) CuZnTe Growth (Stacking fault migration)

Growth of (Cu)ZnTe on the CdTe to complete the (Cu)ZnTe/CdTe/CdS stack reveals several interesting phenomena. Atomistic visualization, structure maps and dislocation maps of the growths with Cu doping levels of stoichiometric 10% and 10% are shown in Figures 33 (a) – (f). In general, there is a preference for the various materials to nucleate into ZB structure for

both doping levels in good agreement with experiment. Clustering is observed in the 10% (Figure 33(d)) but not the stoichiometric 10% (Figure 33 (a)) Cu doping level indicating the importance of stoichiometry during deposition.

There are marked differences in the nature of the CdTe/CdS and (Cu)ZnTe/CdTe interfaces, highlighted by yellow line in Figure 33(b) and €, which may be attributed to their lattice mismatch. The lattice mismatch between CdTe and CdS is ~10% compared to 6% for ZnTe and CdTe. This difference in the lattice mismatch is reflected by the amount of disorder at the interfaces. The CdTe/CdS interface has a higher degree of disorder but less number of dislocations. In contrast, the (Cu)ZnTe/CdTe interfaces are more crystalline but contain more dislocations for both Cu doping levels. This suggest that the materials use different mechanisms to accommodate lattice mismatch; ordered grain boundaries at 10% lattice mismatch, and dislocation formation at the lower 6% lattice mismatch. This is important when considering that disorder at junctions may affect carrier transport and other electronic properties.

Dislocation analysis show that the overall predominant dislocation type is Shockley partial 1/6<112> in both S 10% and 10% Cu sample. However, there are other types of dislocations such as perfect dislocations ½<110>, stair-rod dislocation 1/6<110>, and Frank partial dislocations 1/3<111> throughout the stack. The length of the dislocations in the CdS layer is small compared to those in the CdTe and ZnTe. However, the dislocation density in the (Cu)ZnTe layer is higher compared to the CdTe suggesting that dislocations the ZnTe/CdTe are not completely effective at accommodating the lattice mismatch.

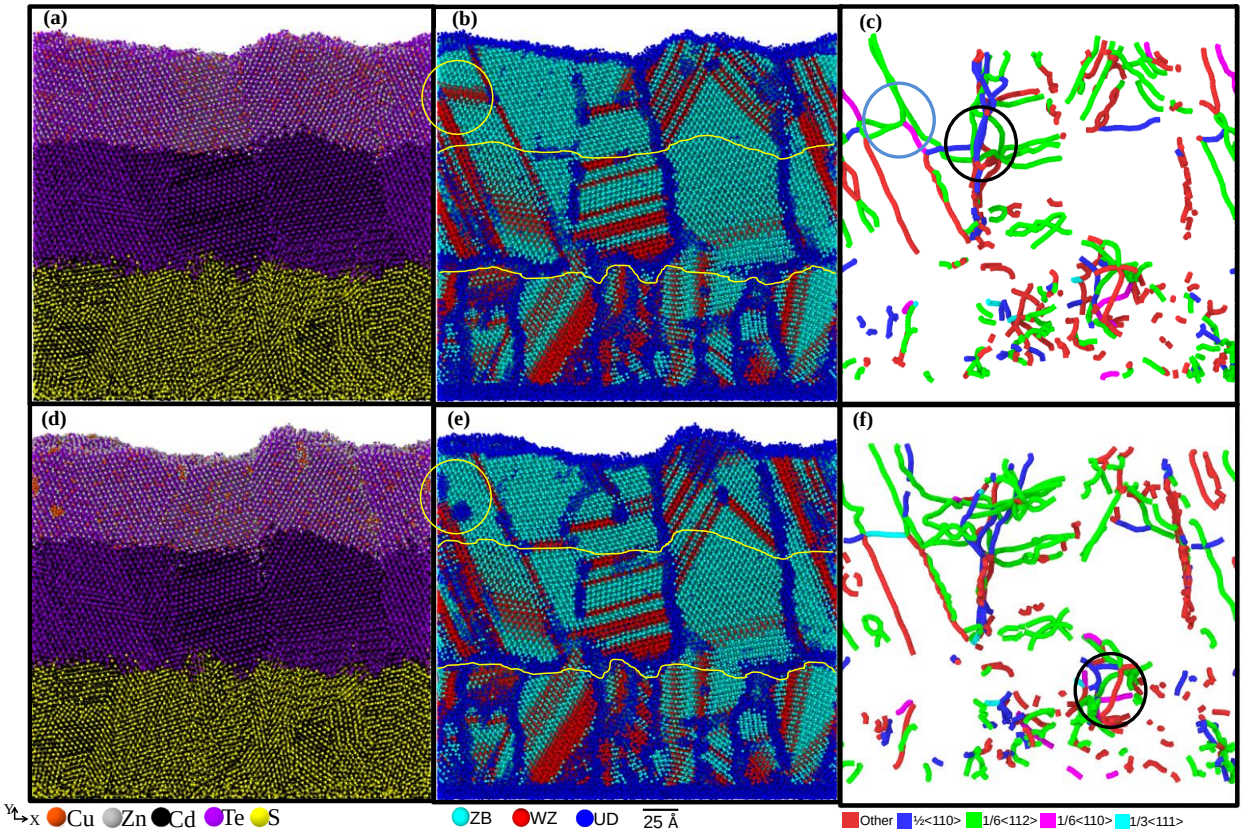

Figure 33: a) Atomistic visualization, b) structural, and c) dislocation map of the sample grown with stoichiometric ratios. Similarly, d) atomistic visualization, e) structural, and f) dislocation map of the polycrystalline sample with 10% Cu.

All the wurtzite regions in Figures 33 (b) and €, which indicate the presence of stacking faults, span the length of the grains with none of them terminating within the grain. However, two instances were observed using time-resolved analysis in which Shockley partial dislocations bounding stacking faults commenced to glide through their respective grain, eliminating the stacking faults. Figure 34 shows the structure maps of the layers at different deposition times depicting the aforementioned phenomena. A pair of stacking faults is indicated by an arrow in Figure 34 (d). However, at ~21.1 ns (Figure 34 (f)), the Shockley partials bounding the stacking faults initiate glide in a manner that reduces the area of the stacking faults. The velocity of the Shockley partials is 0.2 Å/ps which is 2 orders of magnitude faster than the growth rate of the

film. Another example of Shockley partial dislocation glide is observed to initiate at ~26 ns as indicated by the arrow in Figure 34 (g).

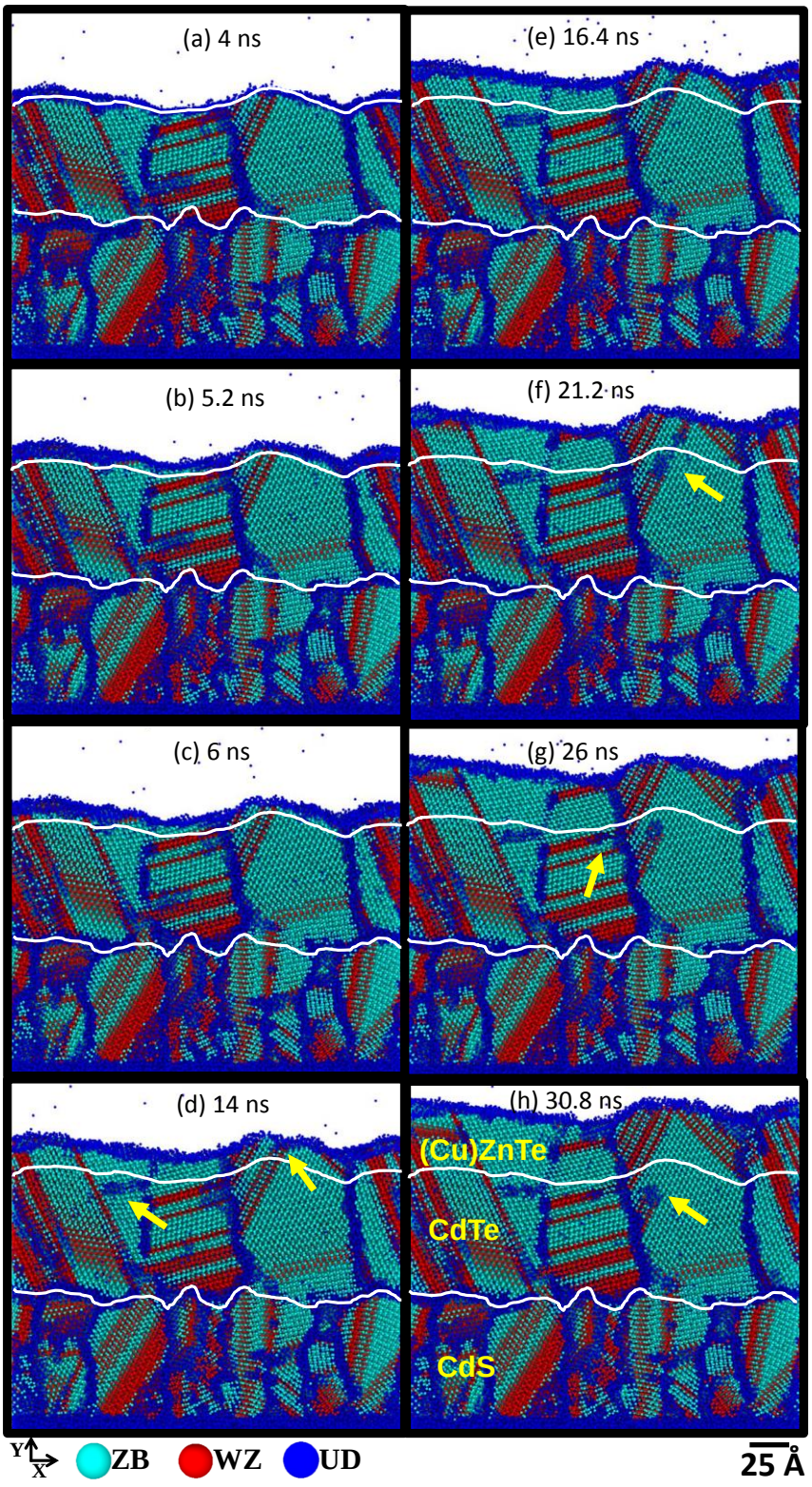

Figure 34: Time evolution structure map during (Cu)ZnTe deposition of the stoichiometric 10% PX sample.

Non-stoichiometry effects the diffusion and incorporation of atoms. In our effort to have a deeper understanding of the incorporation of atoms, localized composition profiles were constructed as shown in Figure 35. The composition profiles are from the center grain for both the S 10% PX and 10% PX samples. Generally, the intermixing between CuZnTe and CdTe layers in the S 10% PX sample can be modeled using a single complementary error function. In contrast, the profile for the 10% PX sample shows more structure such as diffusion tails as shown in Figure 35 (d). This indicates that non-stoichimetry activates diffusion mechanisms not modeled well by a single complementary error function.

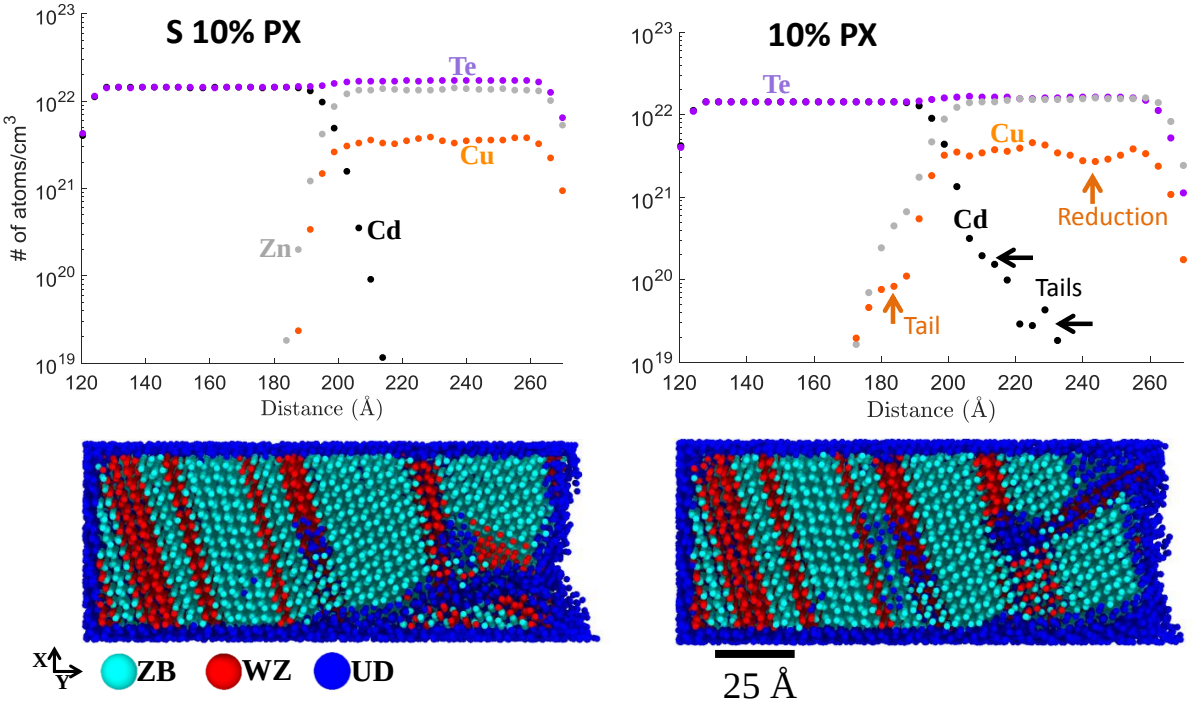

Figure 35: Localized composition profiles at the center grain of the stoichiometric 10% PX and 10% PX samples.

Chapter 5: Conclusion

MD simulations were used to simulate the growth of Cu on single crystal and polycrystalline CdTe heterostructures for the first time.

First, layered growths using single crystal substrates (ZnTe/Cu/SX-CdTe) show Cu cluster formation even at low doses of Cu. Cu clusters are highly mobile and coalescence with other clusters to form bigger clusters of FCC structure over time. Predominantly, WZ structure is observed in the substrate and epilayer. Cu clusters increase diffusion of Cd to the epilayer. Zn and Cu diffusion to the substrate is hardly observed. Shockley partial dislocations are predominant in the substrate, interface and epilayer.

Second, co-evaporated growths using non-stoichiometric vapor rations on single crystal and polycrystalline substrates ((Cu)ZnTe/SX-CdTe and (Cu)ZnTe/PX-CdTe/PX-CdS) also exhibited Cu cluster phenomena while no Cu clusters were observed in the growths using stoichiometric vapor rations. In the non-stoichiometric polycrystalline samples, the Cu clusters diffuse through the grain boundaries. On the other hand, Cd diffusion to the epilayer increases as Cu content increases for both the single crystal and polycrystalline samples. Zn and Cu diffusion to the substrate is enhanced in polycrystalline samples suggesting that defects are generally the driving force for diffusion. Simulated diffusion coefficients of Cu are in good qualitative agreement with experiments in the literature. Predominant structure in the single crystal sample is WZ while in the polycrystalline is ZB. Most dislocations found were Shockley partials for the single crystal samples. On the other hand, for the polycrystalline samples other type of dislocations were found such as perfect dislocations and Frank partial dislocations.

Lastly, polycrystalline heterostructres are in good qualitative agreement with experimental findings. Grain boundary motion was detected during the initial stages of CdTe growth presumably to release strain due to lattice mismatch with the CdS substrate. Also, dislocation glide occurred during the (Cu)ZnTe growth to reduce stacking fault area. The velocity of the dislocation was found to be two times greater the deposition rate.

Chapter 6: Future Work

Future work includes the quantification of grain boundary mobility as described for other compounds in the literature [62]. A set of bicrystals will be artificially constructed with grain boundaries of interest to the scientific community. The grain boundary mobility will be calculated and reported. Also, it is important to identify grain orientations in the simulated polycrystalline growths. An already established approach for fcc and bcc structures [63] will be used for zincblende structures.

References

[1] J. Tsao, N. Lewis and G. Crabtree, "Solar FAQs," 2006.

[2] First Solar , "First solar press release," 16 February 2016. [Online]. Available: http://investor.firstsolar.com/releasedetail.cfm?ReleaseID=956479. [Accessed 1 January 2017].

[3] K. L. Chopra, P. D. Paulson and V. Dutta, "Thin-Film Solar Cells; An Overview," *Progress in Photovoltaics: Research and Applications,* vol. 12, no. 2-3, pp. 69-92, 2004.

[4] P. Sinha, M. de Wild-Scholten, A. Wade and C. Breyer, "Total cost of electricity pricing of photovoltaics," in *28th European Photovoltaic Solar Energy Conference*, Paris, France, 2013.

[5] M. A. Green, K. Emery, Y. Hishikawa, W. Warta, E. D. Dunlop , D. H. Levi and A. W. Y. Ho-Baillie, "Solar cell efficiency tables (version 49)," *Progress in Photovoltaics: Research and Applications,* vol. 25, no. 1, pp. 3-13, 2016.

[6] L. Kranz, C. Gretener, J. Perrenoud, R. Schmitt, F. Pianezzi, F. La Mattina, P. Blosch, E. Cheah, A. Chirila, C. M. Fella, H. Hagendorfer, T. Jager, S. Nishiwaki, A. R. Uhl, S. Buecheler and A. N. Tiwari, "Doping of polycrystalline CdTe for high-efficiency solar cells on flexible metal foil," *nature communications,* 2013.

[7] K. K. Chin, "p-doping limit and donor compensation in CdTe polycrystalline thin film solar cells," *Solar Energy Materials & Solar Cells,* vol. 94, no. 10, pp. 1627-1629, 2010.

[8] J. H. Park, S. Farrell, R. Kodama, C. Blissett, X. Wang, E. Colegrove, W. K. Metzger, T. A. Gessert and S. Sivananthan, "Incorporation and Activation of Arsenic Dopant in Single-Crystal CdTe Grown on Si by Molecular Beam Epitaxy," *Journal of Electronic Materials,* vol. 43, no. 8, pp. 2998-3003, 2014.

[9] J. M. Burst, J. N. Duenow, D. S. Albin, E. Colegrove, M. O. Reese, J. A. Aguiar, C.-S. Jiang, M. K. Patel, M. M. Al-Jassim, D. Kuciauskas, S. Swain, T. Ablekim, K. G. Lynn and W. K. Metzger, "CdTe solar cells with open-circuit voltage breaking the 1V barrier," *Nature Energy,* vol. 1, 2016.

[10] H. R. Moutinho, M. M. Al-Jassim, D. H. Levi, P. C. Dippo and L. L. Kazmerski, "Effects of CdCl2 treatment on the recrystallization and electro-optical properties of CdTe thin films," *Journal of Vacuum Science & Technology A,* vol. 16, no. 3, p. 1251, 1998.

[11] S.-H. Wei, J. Ma, T. A. Gessert and K. K. Chin, "Carrier Density and Compensation in Semiconductors with Multi Dopants and Multi Transition Energy Levels: The Case of Cu Impurity in CdTe," in *37th IEEE Photovoltaic Specialist Conference* , Seattle, Washington, 2011.

[12] A. Stoffers, O. Cojocaru-Miredin, W. Seifert, S. Zaefferer, S. Riepe and D. Raabe, "Grain boundary segregation in multicrystalline silicon: correlative characterization by EBSD, EBIC, and atom probe tomography," *Progress in Photovoltaics: Research and Applications,* vol. 23, no. 12, pp. 1742-1753, 2015.

[13] M. Gloeckler, I. Sankin and Z. Zhao, "CdTe solar cells at the threshold to 20% efficiency," *Journal of Photovoltaics,* vol. 3, no. 4, 2013.

[14] C. Candelise, M. Winskel and R. Gross, "Implications for CdTe and CIGS technologies production costs of indium and tellurium scarcity," *Progress in photovoltaics: research and*

applications, vol. 20, no. 6, pp. 816-831, 2012.

[15] J. Bohland, I. Anisimov and T. Dapkus, "Economic recycling of CdTe photovoltaic modules," in *IEEE PVSC*, Anaheim, CA, 1997.

[16] T. Takahashi and S. Watanabe, "Recent progress in CdTe and CdZnTe detectors," *IEEE Transactions on nuclear science,* vol. 48, no. 4, 2001.

[17] S.-H. Wei and S. Zhang, "Structure stability and carrier localization in CdX (X = S, Se, Te) semiconductors," *Physical review B,* vol. 62, no. 11, 2000.

[18] D. Strauch, "CdTe: lattice parameters," in *Semiconductors - New data and updates for several III-V and II-VI compounds*, 2012, pp. 147-149.

[19] R. W. Birkmire and E. Eser, "Polycrystalline thin film solar cells: Present status and future potential," *Annual review of materials science,* vol. 27, pp. 625-653, 1997.

[20] A. Balcioglu, R. K. Ahrenkiel and F. Hasoon, "Deep-level impurities in CdTe/CdS thin-film solar cells," *Journal of applied physics,* vol. 88, no. 12, 2000.

[21] T. Gessert, J. M. Burst, S.-H. Wei, J. Ma, D. Kuciauskas, W. L. Rance, T. M. Barnes, J. N. Duenow, M. O. Reese, J. V. Li, M. R. Young and P. Dippo, "Pathways toward higher performance CdS/CdTe devices: Te exposure of CdTe surface before ZnTe:Cu/Ti contacting," *Thin Solid Films,* vol. 535, pp. 237-240, 2013.

[22] E. Colegrove, S. P. Harvey, J.-H. Yang, J. M. Burst, D. S. Albin, S.-H. Wei and M. K. Metzger, "Phosphorus Diffusion Mechanism and Deep Incorporation in Polycrystalline and Single-Crystalline CdTe," *Physical Review Applied,* vol. 5, no. 5, 2016.

[23] S.-H. Wei and S. B. Zhang, "Chemical trends of defect formation and doping limit in II-VI semiconductors: The case of CdTe," *Physics Review B,* vol. 66, no. 15, 2002.

[24] D. Krasikov, A. Knizhnik, B. Potapkin, S. Selezneva and T. Sommmerer, "First-principles-based analysis of the influence of Cu on CdTe electronic properties," *Thin Solid Films,* vol. 535, pp. 322-325, 2013.

[25] C. A. Wolden, A. Abbas, J. Li, D. R. Diercks, D. M. Meysing, T. R. Ohno, J. D. Beach, T. M. Barnes and J. M. Walls, "The roles of ZnTe buffer layers on CdTe solar cell performance," *Solar energy materials and solar cells,* vol. 147, pp. 203-210, 2016.

[26] R. Aguirre, J. J. Chavez, X. Zhou, S. F. Almeida and D. Zubia, "Molecular dynamics simulations of ZnTe\Cu back contacts for CdTe solar cells," *IEEE 43rd Photovoltaic Specialist Conference (PVSC),* 2016.

[27] C. Corwine, A. O. Pudov, M. Gloeckler, S. H. Demtsu and J. R. Sites, "Copper inclusion and migration from the back contact in CdTe solar cells," *Solar energy materials & solar cells,* vol. 82, pp. 481-489, 2004.

[28] H. Chou, "Copper migration in CdTe heterojunction solar cells," *Journal of electronic materials,* vol. 25, no. 7, 1996.

[29] V. M. Fthenakis, "Life cycle impact analysis of cadmium in CdTe PV production," *Renewable & sustainable energy reviews,* vol. 8, pp. 303-334, 2004.

[30] J. Luschitz, K. Lakus-Wollny, A. Klein and W. Jaegermann, "Growth regimes of CdTe deposited by close-spaced sublimation for application in thin film solar cells," *Thin film solids,* vol. 515, pp. 5814-5818, 2006.

[31] K. Punitha, R. Sivakumar, C. Sanjeeviraja, V. Sathe and V. Ganesan, "Physical propertiesof electron beam evaporated CdTe and CdTe: Cu thin films," *Journal of applied physics,* vol.

116, 2014.

[32] E. R. Shaaban, N. Afify and A. El-Taher, "Effect of film thickness on microstructure parameters and optical constants of CdTe thin films," *Journal of alloys and compounds,* vol. 482, pp. 400-404, 2009.

[33] C. Buis, E. Gros d'Aillon, A. Lohstroh, G. Marrakchi, C. Jeynes and L. Verger, "Effects of dislocation walls on charge carrier transport properties in CdTe single crystal," *Nuclear instruments and methods in physics research A,* vol. 735, pp. 188-192, 2014.

[34] N. Strevel, L. Trippel, C. Kotarba and I. Khan, "Improvements in CdTe module reliability and long-term degradation through advances in construction and device innovation," Photovoltaics International.

[35] H. Mehrer, "High-diffusivity paths in metals," in *Diffusion in Solids*, 2007, pp. 547-548.

[36] M. Tuteja, P. Koirala, S. MacLaren, R. Collins and A. Rockett, "Direct observation of electrical properties of grain boundaries in sputter-deposited CdTe using scan-probe microwave reflectivity based capacitance measurements," *Applied physics letters,* vol. 107, 2015.

[37] C. Li, Y. Wu, J. Poplawsky, T. J. Pennycook, N. Paudel, W. Yin, S. J. Haigh, M. P. Oxley, A. R. Lupini, M. Al-Jassim, S. J. Pennycook and Y. Yan , "Grain-boundary -enhanced carrier collection in CdTe solar cells," *Physical review letters,* vol. 112, 2014.

[38] C. Li, Y. Wu, T. J. Pennycook, A. R. Lupini , D. N. Leonard, W. Yin, N. Paudel , M. Al-Jassim, Y. Yan and S. J. Pennycook, "Carrier separation at dislocation pairs in CdTe," *Physical review letters,* vol. 111, 2013.

[39] D. A. Porter, "Diffusion along dislocations," in *Phase transformations in metal and alloys*, 2009.

[40] C. Sun, T. Paulauskas, F. G. Sen, G. Lian, J. Wang, C. Buurma, M. K. Y. Chan, R. F. Klie and M. J. Kim, "Atomic and electronic structure of Lomer dislocations at CdTe bicrystal interface," *Scientific Reports,* 2016.

[41] J. Luria, Y. Kutes, A. Moore, L. Zhang, E. A. Stach and B. D. Huey, "Charge transport in CdTe solar cells revealed by conductive tomographic atomic force microscopy," *Nature energy,* 2016.

[42] R. G. Dhere, M. M. Al-Jassim, Y. Yan, K. M. Jones, H. R. Moutinho, T. A. Gessert, P. Sheldon and L. L. Kazmerski, "CdS/CdTe interface analysis by transmission electron microscopy," *Journal of vacuum science & technology,* vol. 18, 2000.

[43] I. M. Dharmadasa, "Review of the CdCl2 treatment used in CdS/CdTe thin film solar cell development and new evidence towards improved understanding," *Coatings,* vol. 4, pp. 282-307, 2014.

[44] Y. Yanfa, K. M. Jones and M. M. Al-Jassim, "Atomic structure of twin boundaries in CdTe," in *National center for photovoltaics and solar program review meeting*, Denver, Colorado, 2003.

[45] D. G. Pettifor and I. I. Oleinik, "Analytic bond-order potentials beyond Tersoff-Brenner. I. Theory," *Physical review B,* vol. 59, no. 13, 1998.

[46] J. E. Jones, "On the determination of molecular fields.-II. From the equation of state of a gas," *Proceedings of the royal society A,* pp. 463-477, 1924.

[47] F. H. Stillinger and T. A. Weber, "Computer simulation of local order in condensed phases

of silicon," *Physicial review B,* vol. 31, p. 5262, 1985.

[48] X. W. Zhou, D. K. Ward, J. E. Martin , F. B. van Swol, J. L. Cruz-Campa and D. Zubia, "Stillinger-weber potential for the II-VI elements Zn-Cd-Hg-S-Se-Te," *Physical review B,* vol. 88, 2013.

[49] F. Ercolessi, "A molecular dynamics primer," Dipartimento di Scienze Matematiche, Informatiche e Fisiche. Univesita degli Studi di Udine, [Online]. Available: http://www.fisica.uniud.it/~ercolessi/md/md/node50.html. [Accessed 26 April 2017].

[50] A. i. Motion, "Atoms in Motion," Atoms in Motion, [Online]. Available: http://atomsinmotion.com/book/chapter5/md. [Accessed 26 4 2017].

[51] R. G. Parr, "Density Functional Theory of atoms and molecules," in *Horizons of Quantum Chemistry*, Spring Netherlands, 1990, pp. 5-15.

[52] J.-H. Yang, W.-J. Yin, J.-S. Park, W. Metzger and S.-H. Wei, "First-principles study of roles of Cu and Cl in polycrystalline CdTe," *Journal of Applied Physics,* vol. 119, 2016.

[53] S. Plimpton, "Fast parallel algorithms for short-range molecular dynamics," *Journal of Computational Physics,* vol. 117, no. 1, pp. 1-19, 1995.

[54] A. Stukowski and K. Albe, "Extracting dislocations and non-dislocation crystal defects from atomistic simulation data," *Modelling and simulation in materials science and engineering,* vol. 18, 2010.

[55] X. W. Zhou, R. E. Jones and J. Gruber, "Molecular dynamics simulations of substitutional diffusion," *Computational materials science,* vol. 128, pp. 331-336, 2017.

[56] M. Ohring, The materials science of thin-films, 1992.

[57] G. Teeter, "The reaction kinetics of Cu with the CdTe(111)-B surface: Formation of metastable CuxTe (x~2)," *The Journal of Chemical Physics ,* vol. 123, 2005.

[58] A. Abbas, D. M. Meysing, J. Li, J. D. Beach, Barnes T. M. , J. M. Walls and C. A. Wolden , "Structural and chemical characterization of the back contact region in high efficiency CdTe solar cells," in *IEEE 42nd Photovoltaic Specialist Conference (PVSC)*, 2015.

[59] Y. Yan, M. M. Al-Jassim, K. M. Jones, S. -H. Wei and S. B. Zhang, "Observation and first-principles calculation of buried wurtzite phases in zinc-blende CdTe thin films," *Applied Physics Letters,* vol. 77, p. 1461, 2000.

[60] D. R. Diercks, J. Li, J. D. Beach, C. A. Wolden and B. P. Gorman, "Atom probe tomography for nanoscale characterization of CdTe device absorber layers and interfaces," *40th IEEE PVSC,* 2014.

[61] B. Gorman, "Hardware and techniques for cross-correlative TEM and atom probe analysis," *Microscopy today,* vol. 16, pp. 42-47, 2008.

[62] K. G. F. Janssens, D. Olmsted, E. A. Holm, S. M. Foiles, S. J. Plimpton and P. M. Derlet , "Computing the mobility of grain boundaries," *nature materials,* vol. 5, pp. 124 - 127, 2006.

[63] J. F. Panzarino and T. J. Rupert, "Tracking Microstructure of Crystalline Materials: A Post-Processing Algorithm for Atomistic Simulations," *The Journal of The Minerals, Metals & Materials Society,* vol. 66, pp. 417-428, 2014.

Vita

Rodolfo Aguirre earned his Bachelor of Engineering degree in Electrical and Computer Engineering from The University of Texas at El Paso in 2011. In 2013, he received his Master of Science degree in Electrical and Computer Engineering from The University of Texas at El Paso. In 2014, he joined the doctoral program in Electrical and Computer Engineering at The University of Texas at El Paso.

Dr. Aguirre was the recipient of numerous honors and awards including the UTEP travel grant and HENAAC award. He was also a recipient of the Solar Economy IGERT grant and the NSF ASSIST travel grant. While pursuing his degree. Dr. Aguirre performed research for a project funded by the Department of Energy. In this project, Dr. Aguirre performed collaboration with scientist from Sandia National Laboratories and Colorado School of Mines to unite efforts for the development and validation of computer simulations to study solar cells.

Dr. Aguirre presented his research at international conference meetings and workshops including the 2017 Material Research Society conference. He authored a conference paper at the 2016 IEEE Photovoltaic Specialist Conference and co-authored a peer-reviewed journal at the Journal of Materials Science Research. Dr. Aguirre's dissertation entitled, "Molecular dynamics studies of crystal growth phenomena in CdTe based heterostructures", was supervised by Dr. David Zubia. Dr. Aguirre is currently seeking for a post-doc position at Sandia National Laboratories.

Contact Information: raguirre4@miners.utep.edu

This thesis/dissertation was typed by Rodolfo Aguirre II